Article

Not peer-reviewed version

Structural, Elastic, Refractive Index and Energy Band Gap Properties of $Li_{0.5}Co_{0.5}FeCrO_4$ Ferrite for Non-Linear Optical and Optoelectronic Applications

Fakher Hcini , Mussad Mohammed Alzahrani , Hcini Hcini , Mohamed Lamjed Bouazizi * , Kamel Khirouni

Posted Date: 8 January 2025

doi: 10.20944/preprints202501.0641.v1

Keywords: spinel ferrite; X-ray diffraction; theoretical optical parameters; sol-gel method; optoelectronic applications

Article

Structural, Elastic, Refractive Index and Energy Band Gap Properties of $Li_{0.5}Co_{0.5}FeCrO_4$ Ferrite for Non-Linear Optical and Optoelectronic Applications

Fakher Hcini [1,2], Mussad Mohammed Alzahrani [3], Sobhi Hcini [1], Mohamed Lamjed Bouazizi [3,*] and Kamel Khirouni [4]

[1] Laboratory of Advanced Multifunctional Materials and Technological Applications, Faculty of Science and Technology of Sidi Bouzid, University Campus Agricultural City, University of Kairouan, 9100 Sidi Bouzid, Tunisia
[2] Advanced Materials, Applied Mechanics, Innovative Processes and Environment Research Unit, Higher Institute of Applied Sciences and Technology of Gabes (ISSATG), University of Gabes, 6072 Gabes, Tunisia
[3] Department of Mechanical and Energy Engineering, College of Engineering, Imam Abdulrahman Bin Faisal University, 1982, Dammam, Saudi Arabia
[4] Laboratory of Physics of Materials and Nanomaterials Applied to the Environment (LaPhyMNE), Faculty of Sciences of Gabès Cited Erriadh, University of Gabès, 6079 Gabès, Tunisia
* Correspondence: lamjedb78@gmail.com

Abstract: This work examines the structural, elastic, and optical properties of the $Li_{0.5}Co_{0.5}FeCrO_4$ spinel ferrite. Rietveld analysis of X-ray diffraction measurement confirms its cubic spinel structure. The structural investigation reveals strong consistency among calculated and refined parameters, validating the proposed cation distribution. Elastic moduli, including bulk, longitudinal, and rigidity moduli, were acquired by computing stiffness constants. Absorbance data and the Tauc method indicated a direct optical transition with a low band-gap energy, suggesting the sample's potential for optoelectronic applications. The $Li_{0.5}Co_{0.5}FeCrO_4$ spinel showed absolutely low Urbach energy, suggesting little disorder and defects within its structure. The theoretical optical characteristics like reflection loss (R_L), polaron radius (R_p), molar refractive index (R_m), molar electronic polarizability (α_m), and the non-linear optical features were examined for our compound. Our findings indicate that the $Li_{0.5}Co_{0.5}FeCrO_4$ compound outperforms the undoped $Li_{0.5}Fe_{2.5}O_4$ compound , featuring a lower band gap. This implies that adding Co and Cr into $Li_{0.5}Fe_{2.5}O_4$ ferrite enhances their optical and optoelectronic applications.

Keywords: spinel ferrite; X-ray diffraction; theoretical optical parameters; sol-gel method; optoelectronic applications

1. Introduction

Spinel ferrites materiels with the typical chemical formula AB_2O_4 (where A, B = Co, Cu, Cr, Ni, Zn, etc.) have been created and researched for their intriguing physical characteristics [1,2]. The accurate tailoring of spinel ferrite characteristics for a variety of applications is made possible by the right synthesis technique, chemical composition, annealing temperature-time, and the nature of doping [3,4]. Numerous scientific and technological applications have been investigated for these, including magnetic memories, high-capacity batteries, electronic-based optical panels and recording media, etc. [3,5,6]. Nanoscale ferrites possess highly adjustable properties, making them ideal for various devices. In addition to their electrical, and magnetic uses, ferrites materials are utilized in visible light absorption, improved photocatalytic performance, and other optical applications [7]. In this case, dielectric and electronic polarizability are crucial parameters that need to be investigated for the effective use of a material in these applications. These characteristics are closely associated with refraction, optical conductivity, the electro-optical effect and optical nonlinearity [8,9]. Materials with a refractive index greater than 2 are beneficial for nonlinear optical applications due to their exceptional optical characteristics. Moreover, many optical characteristics are directly correlated with the refractive index. The physical properties of ferrite compounds can be modified by adjusting factors such as the choice of surfactants, manufacture temperature, and the pH of the solution during the synthesis process [10]. Extensive research documented in the literature highlights recent advancements in the synthesis and applications of ferrite nanoparticles [11]. Several methods have been developed for fabricated spinel ferrite nanoparticles, including sol-gel, co-precipitation, hydrothermal, and microwave combustion techniques [12–14]. Among these, the sol-gel method stands out for its superior control over particle size, composition, purity, and surface morphology [15]. This approach offers several benefits, including producing uniform particle sizes, lowering processing temperatures and annealing times, and allowing precise tuning of chemical mixture [16,17]. Hence, the type and amount of element substitution may be used to adjust the ferrites' characteristics. Numerous studies in this area have been done [18,19].

Lithium ferrite with the formula $Li_{0.5}Fe_{2.5}O_4$ has been widely studied in the literature due to its promising properties. It is a cubic ferrite classified as a soft magnetic material, characterized by a square hysteresis loop, high Curie temperature, and strong magnetization [20,21]. Its versatile properties enable various technological applications, including use in microwave devices, magnetic recording, transformer cores, antenna rods, ferrofluids, hyperthermia treatment, and as a potential cathode material in lithium-ion batteries [22–24]. Various studies and review papers have examined the properties of different spinel ferrites, including lithium-based ferrites such as Li-Co [25], Li-Zn [26], Li-Mg [27], and Ni-Li [28]. In these investigations, several substitutions have been made in $Li_{0.5}Fe_{2.5}O_4$ sample to improve its practical applications [29,30].

This article also discusses the physical properties of lithium ferrite $Li_{0.5}Fe_{2.5}O_4$ with Co-Cr substitution. Such substitution alters the crystal structure, which in turn affects the optical and elastic properties of the sample. Previous studies have shown that replacing Co and Cr ions in spinel ferrites introduces energy levels within the band gap, leading to a reduction in band-gap energies, which enhances their performance in optoelectronic technology [31–33]. Nevertheless, the elastic , lattice energy, structural characteristics, and related parameters of $Li_{0.5}Co_{0.5}FeCrO_4$ have been theoretically computed and extensively discussed using derived structural and optical data. Using the structural parameters and the experimentally determined optical band gap, several optical factors for our sample have been estimated theoretically and are thoroughly explained in this paper. These calculations offer a comprehensive guide for researchers to prepare the desired $Li_{0.5}Co_{0.5}FeCrO_4$ sample for optical and optoelectronic applications. Additionally, the non-linear optical parameters obtained for our sample are in good agreement with those reported for other materials that are considered strong candidates for nonlinear applications.

2. Experimental Details

The $Li_{0.5}Co_{0.5}FeCrO_4$ sample was produced by the sol-gel route. Fig 1 is depicted the synthesis step. Primarily, nitrates [$Co(NO_3)_2.6H_2O$], [$Li(NO_3)$], [$Fe(NO_3)_2.9H_2O$] and [$Cr(NO_3)_3.9H_2O$]), all possessing a purity greater than 99%, were dissolved in deionized water and subjected to stirring on a hot plate set to 90 °C. Following the full dissolution of the nitrate, exact quantities of citric acid were introduced as a complexing agent, and the pH was adjusted to approximately 7 using ammonia. Then, to make a thick gel-like solution, ethylene glycol was added. The gel was heated to 250 °C, resulting the formation of a brown foam that was later ground with an agate mortar. The formed powder was thermally treated at 600 °C for 12 hours to remove any organic residues. It was subsequently ground and exposed to calcination at 800 °C for 12 hours. After this step, the powder was ground, and an XRD analysis was performed following heating at 800 °C to confirm the purity of the prepared specimen. However, since the powder remained partially non-uniform at this temperature, the calcination temperature was raised to 1000 °C, leading to the successful formation of the desired crystalline phase. In this work, the characterization findings of $Li_{0.5}Co_{0.5}FeCrO_4$ ferrite calcined at 1000 °C are then presented.

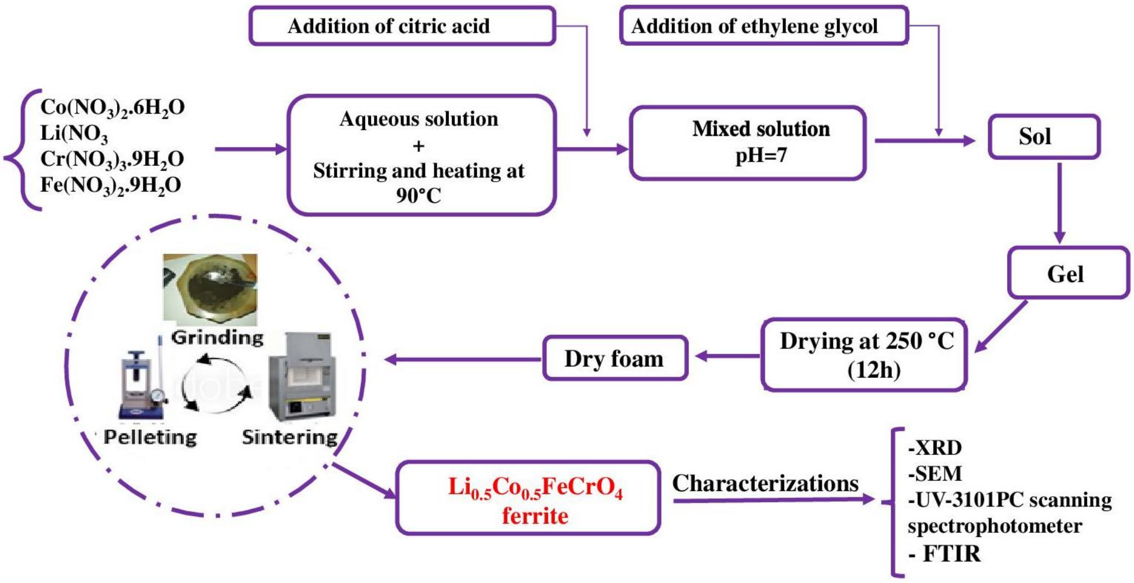

Figure 1. Different synthesis steps of using the sol-gel method.

The X-ray diffraction (XRD) data was acquired with a Panalytical X'Pert Pro instrument, employing an angular step of 0.02°. The morphology of the $Li_{0.5}Co_{0.5}FeCrO_4$ sample was investigated with scanning electron microscopy (SEM: JSM-6380 LA). The spectral data from FTIR were acquired with an FTIR-8400S spectrometer, covering the range of 400 cm^{-1} to 1000 cm^{-1} with a resolution of 1 cm^{-1}. The absorbance data was acquired using a UV-Vis spectrophotometer over a wavelength range of 400 nm to 1000 nm, with a step size of 1 nm.

3. Results and Discussions

3.1. Structural Properties

3.1.1. Rietveld Refinement

The X-ray diffraction (XRD) pattern of the produced $Li_{0.5}Co_{0.5}FeCrO_4$ ferrite is plotted in Fig. 2. The diffraction peaks indicate that the specimen possesses a cubic spinel structure with $Fd\bar{3}m$ space group. The pattern reveals uniform crystallization of the produced powder, demonstrating a pure phase with no additional phases present. The clear peaks in Fig. 2, such as (111), (220), (311), (222), (400), (422), (511), (440), (531), (620), (533), (622) and (444) are all correlated with the cubic spinel structure. Using formula (1) [34] we estimated the experimental lattice constant denotes as "a_{exp}".

$$a_{exp} = d_{hkl}\sqrt{h^2 + k^2 + l^2} \qquad (1)$$

$$2d_{hkl}\,sin\,\theta_{hkl} = \lambda \qquad (2)$$

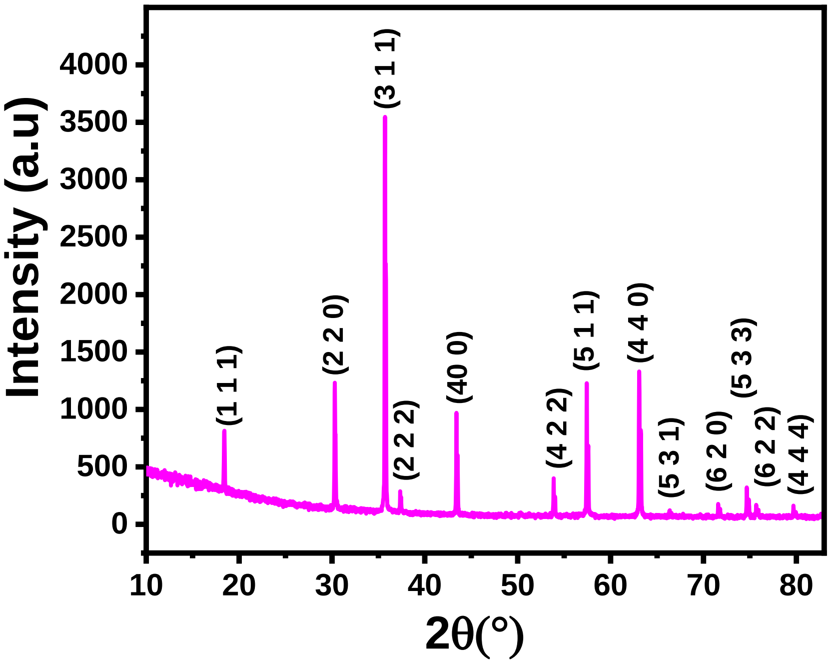

Figure 2. XRD pattern of $Li_{0.5}Co_{0.5}FeCrO_4$ ferrite. All peaks are indexed in the cubic spinel type structure ($Fd\overline{3}m$ space group).

Here, (*hkl*) stands for the miller indices of the (311) X-ray Bragg peak. It is noted that the lattice constant of our sample exceeds that of the parent $Li_{0.5}Fe_{2.5}O_4$ ferrite [35,36], which is attributed to the increased average radius of the B site caused by the adding of Co and Cr ions in the $Li_{0.5}Fe_{2.5}O_4$ structure. Furthermore, a detected elevation in the lattice parameters, *a* and *V* of the $Li_{0.5}Co_{0.5}FeCrO_4$ sample, compared to the undoped $Li_{0.5}Fe_{2.5}O_4$ sample, can be explained by the growth in crystallite size. As the crystallite size grows, the strain energy within the crystal lattice diminishes, permitting the lattice to expand and to allow the larger crystallites. Therefore, the rise in lattice parameters directly results from the growth in crystallite size. Evaluating the cation positions within the A and B sites is essential for analyzing the XRD pattern of $Li_{0.5}Co_{0.5}FeCrO_4$. Research suggests that in ferrites with Co, Fe, Li, and Cr, Li^+, $Cr^{3+}$and Co^{2+} ions occupy the B sites, with Fe^{3+} ions distributed across both sites [37–39]. In addition, the cation distribution for $Li_{0.5}Co_{0.5}FeCrO_4$ compound can be described as $(Fe_1^{3+})_A[Li_{0.5}^{+}Co_{0.5}^{2+}Cr_1^{3+}]_B O_4^{2-}$. The refined structural parameters were reviewed and shown in Table 1. The findings indicated that the refined occupancy factors for Fe in the A-site, and for Co, Cr, and Li in the B-site, were in good agreement with the nominal values, confirming the proposed cation distribution. Figure 3 presents a correlation between the computed and observed patterns, highlighting their agreement. The Rietveld refinement allocated the B cations, A cations, and oxygen to the specific locations 16d (1/2,1/2,1/2), 8a (1/8,1/8,1/8), and 32e (x, y, z), respectively. The R-factors (structural R_F, profile R_P, and weighted profile R_{wp}) were below 10 % and the goodness of fit (χ^2) was close to one, confirming the reliability of the Rietveld fitting analysis. Here, the Oxygen's atomic placement (0.2590 (5)) matches up with the usual properties of a spinel-like structure.

Table 1. Calculated and refined structural parameters for $Li_{0.5}Co_{0.5}FeCrO_4$ ferrite sample.

		Theoretical values	**Refined values**
Space group		**$Fd\overline{3}m$**	
Cell parameters	***a*** **(Å)**	8.33	8.341 (3)
	V **(Å^3)**	578	580.30 (2)
Oxygen parameter	*u*	0.3919	0.387
Oxygen parameter deviation	*δ*	0.0169	0.012

Atoms	**Tetrahedral A site (Fe)**	r_{tet} **(Å)**	0.67	-
		Atomic positions $x=y=z$	1/8	1/8
		B_{iso} **(Å^2)**	-	1.727 (1)
	Octahedral B site ($Li_{0.5}/Co_{0.5}/Cr_1$)	r_{oct} **(Å)**	1.41	-
		Atomic positions $x=y=z$	1/2	1/2
		B_{iso} **(Å^2)**	-	0.742 (1)
	O	**Atomic positions** $x=y=z$	-	0.2590 (5)
		B_{iso} **(Å^2)**	-	0.814 (1)
Hopping lengths	L_A (Å)		3.61	3.6194 (2)
	L_B (Å)		2.9479	2.951 (2)
Bond lengths	d_{AL} (Å)		2.05	1.998 (2)
	d_{BL} (Å)		1.9534	1.9589 (3)
Tetrahedral edge length	$d_{AE(O-O)}$ (Å)		3.3476	3.3503(2)
Shared octahedral edge length	$d_{BE(O-O)}$ (Å)		2.5482	2.552 (1)
Unshared octahedral edge length	$d_{BEU(O-O)}$ (Å)		2.9614	2.970 (2)
Me–Me distances (Å)	b_{B-B}		2.9471	2.9497 (2)
	c_{A-B}		3.4567	3.4531 (2)
	d_{A-A}		3.61	3.621 (1)
	e_{A-B}		5.4156	5.4197 (2)
	f_{B-B}		5.1059	5.1172 (3)
Me–O distances (Å)	p_{B-O}		1.9431	1.9543 (2)
	q_{A-O}		2.05	2.03 (2)
	r_{A-O}		3.93	3.942 (2)
	s_{B-O}		3.692	3.685 (4)
Bond angles (°)	θ_{A-O-B}		119.893	120.05 (2)
	θ_{A-O-B}		145.68	145.45(2)
	θ_{B-O-B}		98.7	98.85 (2)
	θ_{B-O-B}		125.142	125.95 (4)
	θ_{A-O-A}		72.882	72.95 (2)
Agreement factors	R_p (%)		-	6.59
	R_{wp} (%)		-	8.73
	R_F (%)		-	4.98
	χ^2 (%)		-	1.14

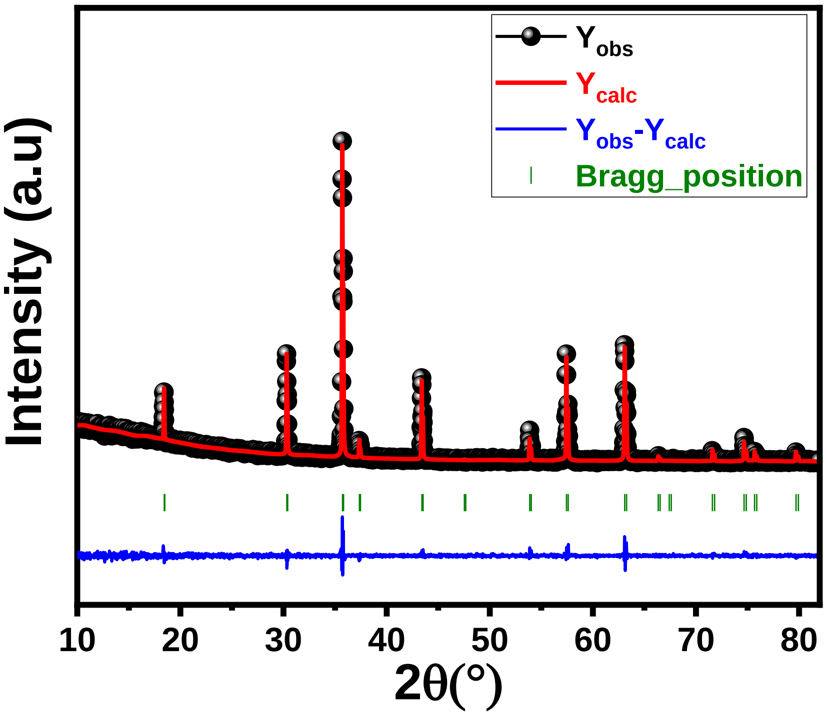

Figure 3. XRD pattern with Rietveld refinement for $Li_{0.5}Co_{0.5}FeCrO_4$ ferrite.

The X-ray density of our specimen was computed by the following formula [40]:

$$\rho_{XRD} = \frac{8M}{N_A a^3} \tag{3}$$

Here, N_A is the Avogadro's number. The ρ_{XRD} value for the $Li_{0.5}Co_{0.5}FeCrO_4$ sample is determined to be 4.678 g.cm^{-3}. The Scherer formula [40] was served to compute the average crystallite size from the XRD peaks, as follows:

$$D = \frac{0.9\,\lambda}{\beta\,cos(\theta)} \tag{4}$$

Here, λ= 1.5406 Å stands for the X-ray wavelength, β denotes the full width at half maximum of the peak with the highest intensity, θ is the Bragg angle. This equation provided a D value roughly 39 nm for $Li_{0.5}Co_{0.5}FeCrO_4$ sample.

3.1.2. Theoretical Structural Parameters

The stated cation distribution for the $Li_{0.5}Co_{0.5}FeCrO_4$ specimen serves to compute the theoretical value of lattice constant (ath) as follows [41]:

$$a_{th} = \frac{8}{3\sqrt{3}}\left[(r_{tet} + r_O) + \sqrt{3}(r_{oct} + r_O)\right] \tag{5}$$

Here, the ionic radius of oxygen is denoted by r_O = 1.38 Å [42], while the ionic radii of the A and B sites are denoted by r_{tet} and r_{oct}, respectively. So, formulae (6) and (7) were employed to acquire the r_{tet} and r_{oct} radii for each location.

$$r_{tet} = r_{Fe^{3+}} \tag{6}$$

$$r_{oct} = \frac{1}{2}[\,0.5\,r_{Co^{2+}} + 0.5\,r_{Li^{+}} + 1\,r_{cr^{3+}}] \tag{7}$$

Shannon's study [43] was referenced in order to ascertain the ionic radii values for the various cations that occupy the A and B locations. The values of r_{tet}, r_{oct}, and ath are listed in Table 1.

As depict from Table 1, the refined (a_{ref}) constant is contrasted with the theoretical a_{th} constant. This suggested cation distribution is accurate, which seen by the remarkable agreement between the (a_{ref}) and a_{th} lattice constants. Utilizing formula (8) is used to compute the value of the oxygen placement parameter "u" from the theoretical lattice constant [41]:

$$u = \left[\frac{1}{\sqrt{3}a_{th}}(r_{tet} + r_O) + \frac{1}{4}\right] \tag{8}$$

The generated "u" value as around 0.3919 , which slightly surpasses the ideal value for a cubic spinel structure ($u_{ideal} = 0.375$). This inconsistency indicates a possible shift of the oxygen anion from its ideal location, suggesting a minor lattice distortion in the $Li_{0.5}Co_{0.5}FeCrO_4$ sample. The small modification within the predicted oxygen parameter is reflected by [δ= u-0.375= 0.0169].

The hopping lengths (L_A) and (L_B) are vital for searching the interionic distances across magnetic ions situated at A and B locations, which directly impact the strength of spin interactions. Stanley's formulae offer a method for calculating these parameters [41]:

$$L_A = \frac{a_{th}\sqrt{3}}{4} \tag{9}$$

$$L_B = \frac{a_{th}\sqrt{2}}{4} \tag{10}$$

The following formulae are utilized to calculate the tetrahedral and octahedral bond lengths denotes as (d_{AL} and d_{BL}), the tetrahedral edge length (d_{AE}), as well as the shared (d_{BE}), and unshared (d_{BEU}) octahedral edge lengths **[**41**]**. For our specimen, these distances are determined using the *ath* and u parameters relying on the corresponding formulae:

$$d_{AL} = a_{th}\sqrt{3}\left(u - \frac{1}{4}\right) \tag{11}$$

$$d_{BL} = a_{th}\sqrt{3u^2 - \frac{11}{4}u + \frac{43}{64}} \tag{12}$$

$$d_{AE} = a_{th}\sqrt{2}\left(2u - \frac{1}{2}\right) \tag{13}$$

$$d_{BE} = a_{th}\sqrt{2}(1 - 2u) \tag{14}$$

$$d_{BEU} = a_{th}\sqrt{4u^2 - 3u + \frac{11}{16}} \tag{15}$$

Table 1 lists the assigned d_{AL}, d_{BL}, d_{AE}, d_{BE}, and d_{BEU} distances for the $Li_{0.5}Co_{0.5}FeCrO_4$ sample. Cation-anion (p, q, r, and s), cation-cation (b, c, d, e, and f) and bond lengths in spinels were utilized to compute bond angles (θ_1 to θ_5) [41].

In spinel structures, metal cations at A location and B site form three main super-exchange interactions type: A-A, B-B, and A-B, classified into five types based on bond angle changes with oxygen ions. angles θ_1 and θ_2 are akin to A-O-B type interactions, angles θ_3 and θ_4 to B-O-B interactions, and θ_5 to A-O-A interactions. Cation-cation (Me-Me) distances, cation-anion (Me-O) distances, and bond angles (Me-O-Me) were obtained as follows [44]**:**

$$b = \frac{a_{th}\sqrt{2}}{4} c = \frac{a_{th}\sqrt{11}}{8} \quad d = \frac{a_{th}\sqrt{3}}{4} \quad e = \frac{3\sqrt{3}a_{th}}{8} \quad f = \frac{a_{th}\sqrt{6}}{4} \tag{16}$$

$$p = a_{th}\left(\frac{5}{8} - u\right) \quad q = a_{th}\sqrt{3}\left(u - \frac{1}{4}\right) \quad r = a_{th}\sqrt{11}\left(u - \frac{1}{4}\right) \quad s = a_{th}\sqrt{3}\left(\frac{u}{3} + \frac{1}{8}\right) \tag{17}$$

$$\theta_1 = cos^{-1}\left(\frac{p^2 + q^2 - c^2}{2pq}\right) \tag{18}$$

$$\theta_2 = cos^{-1}\left(\frac{p^2 + r^2 - e^2}{2pr}\right) \tag{19}$$

$$\theta_3 = cos^{-1}\left(\frac{2p^2 - b^2}{2p^2}\right) \tag{20}$$

$$\theta_4 = cos^{-1}\left(\frac{p^2 + s^2 - f^2}{2ps}\right) \tag{21}$$

$$\theta_5 = cos^{-1}\left(\frac{r^2 + q^2 - d^2}{2qr}\right) \tag{22}$$

In line with the findings as shown in Fig. 4, the findings are reported in Table 1, which highlights the predominance of A-B interactions.

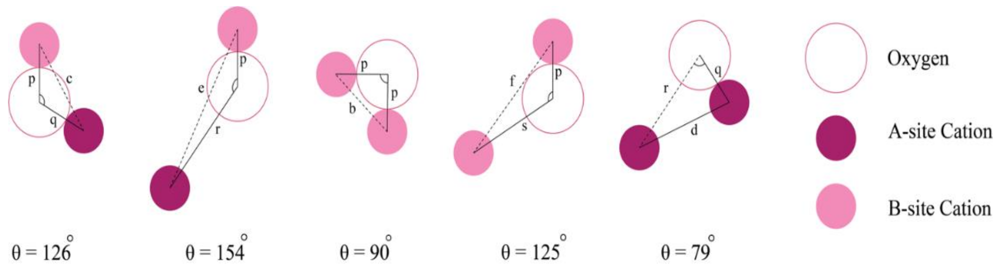

Figure 4. Favorable interionic distances and angles in $Li_{0.5}Co_{0.5}FeCrO_4$ ferrite spinel for better magnetic interaction.

3.2. Morphological Analysis

The SEM study of $Li_{0.5}Co_{0.5}FeCrO_4$ ferrite is displayed in Fig 5a. Grain homogeneity is seen in the SEM micrograph. Additionally, Fig 5a shows how the calcination temperature around 1000 °C affects the particle morphology. Due to the electrostatic magnetic attraction and the effects of high-temperature calcination, individual nanoparticles fully aggregated, and the resulting micrograph revealed clusters of agglomerated ferrites particles. Fig 5b depict the Gaussian-fitted histogram of our sample. Image analysis indicated grain size of approximately 0.51 µm for the prepared sample. In our case, the grain size value derived from the SEM micrograph is larger than those inferred from the XRD data. This discrepancy arises because each grain observed in the SEM image consists of multiple crystallite domain [45].

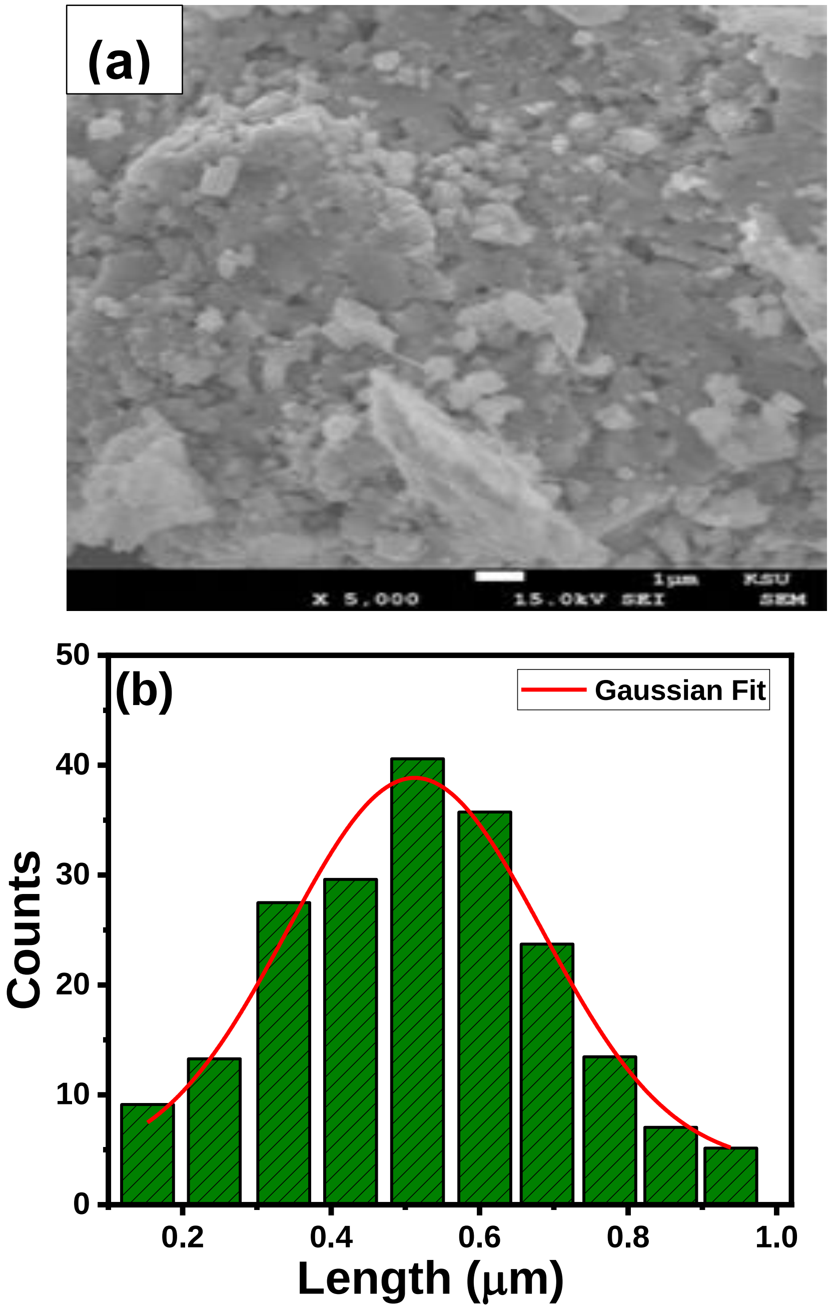

Figure 5. **(a)** SEM image for $Li_{0.5}Co_{0.5}FeCrO_4$ ferrite sample. **(b)** Grain size distribution.

3.3. Infrared and Elastic Properties

3.3.1. FTIR Spectra Analysis

Ferrites materiels are considered as attached crystals, where atoms are connected to their nearest neighbors through equivalent forces such as ionic, covalent, or Van der Waals interactions [46]. Due to the geometric arrangement of nearby oxygen atoms, spinel ferrites consist of metal ions occupying two distinct sublattices: the (A)-location and [B]-site. In this structure, tetrahedral ions vibrate along the line connecting the cation to adjacent oxygen atoms, while octahedral cations oscillate in a direction perpendicular to the axis linking the tetrahedral metal ion and oxygen atom [47]. Fig 6 presents the infrared spectrum of $Li_{0.5}Co_{0.5}FeCrO_4$ ferrite. This graph shows two absorption bands corresponding to metal-oxide vibrational modes [48,49]. The band near 600 cm^{-1} is linked to tetrahedral group stretching (υ_A), while the one around 452 cm^{-1} is associated with octahedral metal-oxygen stretching (υ_B), confirming the formation of metal-oxide bonds (Fe-O and Li, Co, Cr, Fe-O).

Furthermore, compared to the undoped $Li_{0.5}Fe_{2.5}O_4$, replacing Co and Cr in our sample grows the (υ_A) band from 447 cm^{-1} to 452 cm^{-1} and the (υ_B) band from 571 cm^{-1} to 615 cm^{-1} [35]. This change is probably caused by variations in the size of the crystallites and the distribution of cations throughout octahedral and tetrahedral locations [50].

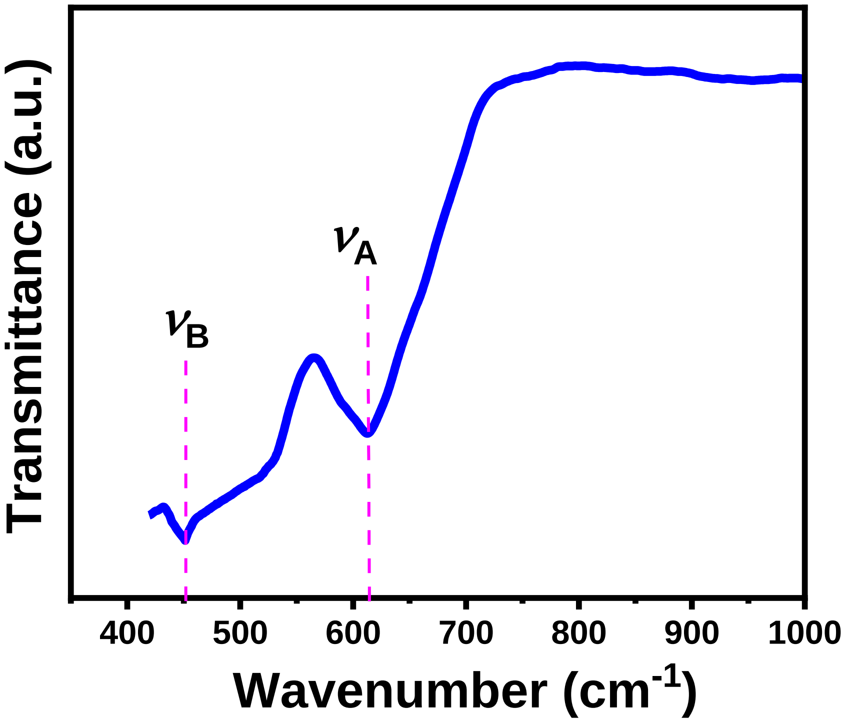

Figure 6. FTIR spectra for $Li_{0.5}Co_{0.5}FeCrO_4$ ferrite sample.

3.3.2. Elastic and Thermal Properties

Ferrites samples possess notable elastic and thermal results due to interatomic and interionic forces. Ultrasonic pulse transmission is commonly used to determine elastic constants and Debye temperatures [51]. Studies have explored links between the structural parameters, and FTIR data. In this case, Modi et al. introduced a method for analyzing spinel ferrite elasticity using FTIR data [52]. In the infrared radiation phonon mode, the wavenumbers denote as ν_A and ν_B are precisely proportional to the force constants (K_t) linked to A location and (K_o) for the octahedral B site. To find these parameters, the Waldron formulae were utilized [53]:

$$K_t = 7.62 \times M_A \times \nu_A^2 \times 10^{-7} \tag{23}$$

$$K_o = 10.62 \times (\frac{M_B}{2}) \times \nu_B^2 \times 10^{-7} \tag{24}$$

Employing the cation distribution formula for our specimen, the molecular weights M_A and M_B of the cations at sites A and B are computed. Table 2 presents the average force constant ($K_{av} = \frac{K_t+K_o}{2}$) as well as the determined force constants. Given the connection among force constants and bond lengths, the obtained K_t value in the $Li_{0.5}Co_{0.5}FeCrO_4$ sample is substantially higher than K_o value [54]. Further, compared to the undoped $Li_{0.5}Fe_{2.5}O_4$ sample, the average force constant K_{av} for our compound grows with the substitution of Co and Cr ions [35]. Hooke's law, which depends on the stress-strain relationship, connects the stress σ_i, the strain ε_{ij}, and the stiffness coefficients C_{ij} [55]. These stiffness coefficients are crucial for determining the elastic constants. In materials with cubic symmetry, only three stiffness coefficients are considered significant. Among them: C_{11}, which represents the elasticity associated with length changes, is linked to the average force constant (K_{av}) and the unit cell parameter "a" through a specific formula [54].

$$C_{11} = \frac{k_{av}}{a} \tag{25}$$

Table 2. Elastic and thermal parameters for $Li_{0.5}Co_{0.5}FeCrO_4$ ferrite sample.

Sample		**$Li_{0.5}Co_{0.5}FeCrO_4$**
Absorption bands (cm^{-1})	υ_B	452
	υ_A	615
Force constant (N m^{-1})	K_t	161.57
	K_o	158.94
	K_{av}	160.25
Stiffness constant (GPa)	C_{11}	193.31
	C_{12}	64.43
	C_{44}	81.45
Wave velocity (ms^{-1})	υ_l	6422.27
	υ_t	3707.903
	υ_m	3923.24
Longitudinal modulus (GPa)	L	192.30
Rigidity modulus (GPa)	G	63.34
Bulk modulus (GPa)	B	107.39
Poisson's ratio	σ	0.25
Pugh ratio	B/G	1.695
Debye temperature (K)	θ_D	558.54
Thermal conductivity (W/m.K)	K_{min}	1.178

However, C_{12} and C_{44}, which possess shape-altering elasticity, are delivered by [54]:

$$C_{12} = \frac{\sigma\, C_{11}}{1-\sigma} \tag{26}$$

$$C_{44} = \rho^2 v_t \tag{27}$$

In this context, ρ stands for the X-ray density. The parameters above, including the transverse wave velocity v_t, the longitudinal wave velocity v_l and the Poisson's ratio σ, were computed using these formulae [56].

$$v_t = \frac{v_l}{\sqrt{3}} \tag{28}$$

$$v_l = \sqrt{\frac{C_{11}}{\rho}} \tag{29}$$

$$\sigma = \frac{L-2G}{2(L-G)} \tag{30}$$

Here, the lengthwise and rigidity moduli are denoted by $L = \rho\, v_l^2$ and $G = \rho\, v_t^2$, respectively. A material's resistance to shearing pressures is measured by its shear modulus (L), yet its resistance to compression or stretching forces is shown by its longitudinal modulus (G). Table 2 defines values for C_{11}, C_{12}, C_{44}, v_t, v_l, L, G, and σ. So far, when energy transfer leads to particle vibrations, shear waves travel more slowly than longitudinal waves. Particles in shear waves vibrate perpendicular to the direction of the wave, requiring more energy to cause vibrations in neighboring particles [57]. According to isotropic elasticity theory, the Poisson's ratio σ, which ranges from -1 to 0.5, aids in estimating brittleness and ductility [58]. The Pugh law determines ductility or brittleness by computing the bulk modulus-to-shear modulus ratio [B/G] [59], where ($B = \frac{1}{3}(C_{11} + 2C_{12})$. If ($B/G$) above 1.75 indicates ductility, while below 1.75 suggests brittleness. The Debye temperature denotes

doi:10.20944/preprints202501.0641.v1

"θ_D" estimated using Anderson's formula above [56], reflects maximum lattice vibrations and provides insight into thermodynamic properties and heat transfer [56]:

$$\theta_D = \frac{\hbar}{k_B}\left(\frac{3q\rho N_A}{4\pi M}\right)^{\frac{1}{3}} \nu_m \tag{31}$$

Here, $\hbar$ stands for Planck's constant, q denotes the number of atoms per formula unit , k_B for Boltzmann's constant, ρ stands for density, N_A for Avogadro's number, and M for molecular mass. For scientists, to appreciate how energy moves through a material, the mean wave velocity denotes (ν_m), is acquired as follows :

$$\nu_m = \left(\frac{1}{3}\left(\frac{2}{\nu_t^3} + \frac{1}{\nu_l^3}\right)\right)^{-1/3} \tag{32}$$

The capacity of a material to transfer heat is measured by its thermal conductivity, reported as a crucial thermodynamic characteristic. The above formula can be used to compute the minimal thermal conductivity (K_{min}) for our specimen **[56]**.

$$K_{min} = \left(\frac{M}{q\rho N_A}\right)^{-\frac{2}{3}} k_B \nu_m \tag{33}$$

Table 2 gives the measured values of θ_D, ν_m, and K_{min}. By evaluating our findings with the undoped $Li_{0.5}Fe_{2.5}O_4$ compound, we find that the obtained ν_m value is higher for $Li_{0.5}Co_{0.5}FeCrO_4$, while the Debye temperature θ_D is lower [35]. The increase in ν_m can be attributed to the higher transverse and longitudinal wave velocities observed in our specimen. Nonetheless, the reduced bonding strength within our ferrite could be the cause of the drop in Debye temperature [60].

3.4. Optical Properties

3.4.1. UV-VIS-NIR Absorbance and Reflectance Spectra

Figure 7 (a, b) appears the absorption $A(\lambda)$ measurement and reflectance $(R(\lambda))$ data of our specimen. The $A(\lambda)$ measurement signaling that our compound has strong UV-VIS light absorption capability. Thus, it is a desirable choice for photovoltaic solar cells and photo-catalysis compounds [61,62]. Additionally, the observed NIR absorption bands suggest its potential for use in NIR optoelectronic devices [63].

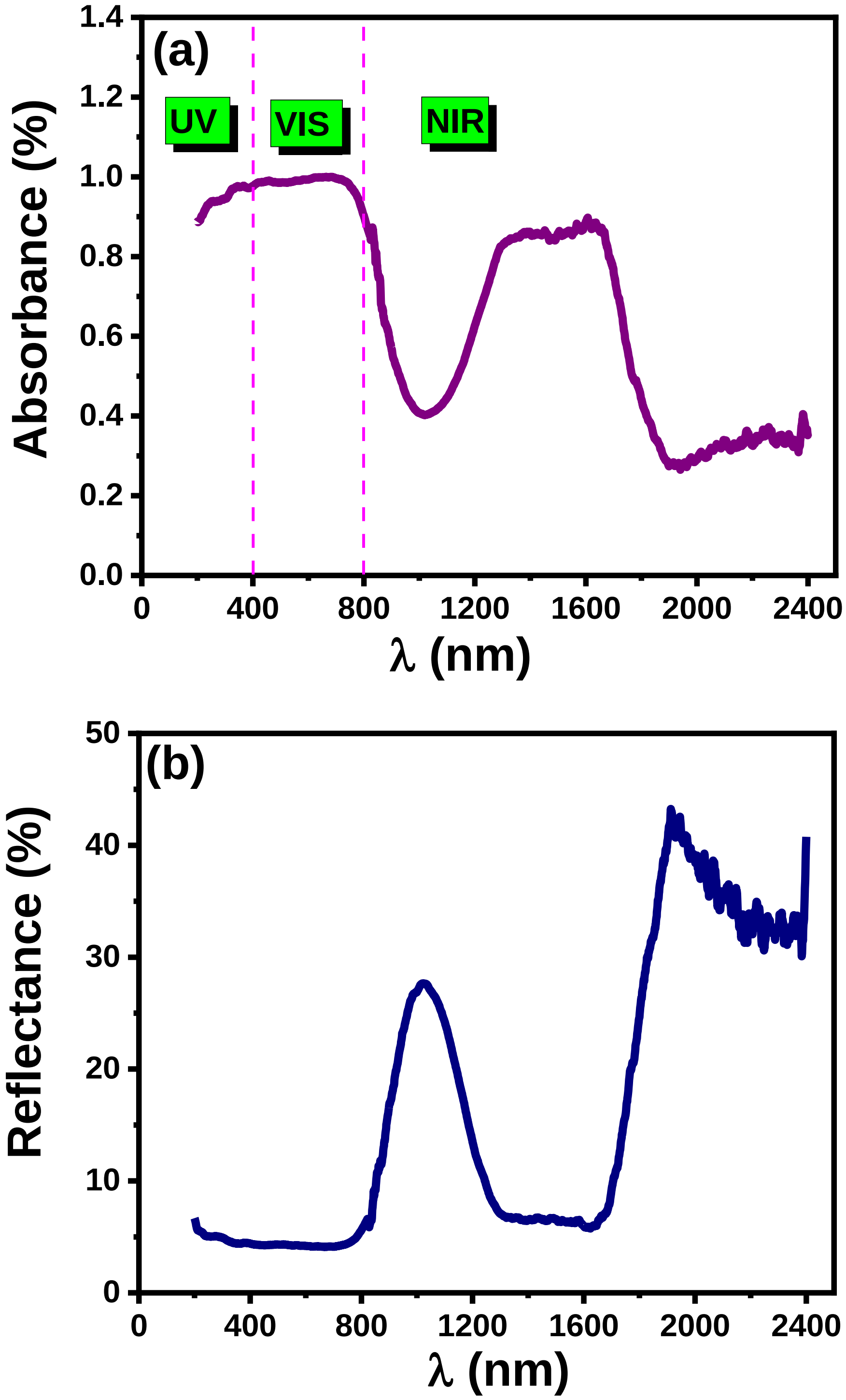

Figure 7. (a) UV–VIS-NIR absorbance spectra versus wavelength for $Li_{0.5}Co_{0.5}FeCrO_4$ ferrite sample. **(b)** Reflectance spectrum $R(\lambda)$.

3.4.2. Optical Energy Band Gap (E_g)

The optical energy band gap denotes as "E_g" is a crucial parameter for ferrites materials, enhancing their suitability for photosensitive device applications. It represents the minimum energy required for the material to absorb incident photons. In this study, the E_g value is find by Tauc's rule in the following way [64].

$$\alpha h\nu = \beta(h\nu - E_g)^n \tag{34}$$

In this context, E_g represents the band-gap energy, $h\nu$ denotes the photon energy, and β denotes a parameter. The exponent n specifies the nature of optical transition, this : an indirect optical transition for $n = 2$ and a direct optical transition for $n = 1/2$. In our research , the optical absorption coefficient (α) is found based formula. (35). As well , the band gap energy (E_g) for $Li_{0.5}Co_{0.5}FeCrO_4$ compound is gets determined by the Tauc theory establish in Eq. (36) [63]. To further confirm the optical transition type in the specimen , Eq. (37) is also applied.

$$\alpha = \frac{2.303\times A}{d} \tag{35}$$

$$(\alpha h\nu)^{1/n} = \beta(h\nu - E_g) \tag{36}$$

$$\ln(\alpha h\nu) = \ln(\beta) + n\ln(h\nu - E_{gd}) \tag{37}$$

Here A denotes the absorbance, d is the thickness of $Li_{0.5}Co_{0.5}FeCrO_4$ compound, and $h\nu$ seems for the photon energy. Relying the $(\alpha h\nu)^2$ versus $h\nu$ spectrum apparent in Fig. 8.a, for our specimen the direct (E_{gd}) band gap value was came out to be 1.85 eV. The $\ln(\alpha h\nu)$ against. $\ln(h\nu\text{-}E_g)$ plot in Fig. 8.b suggests that the exponent n is close to 0.5 for our compound , conveying that $Li_{0.5}Co_{0.5}FeCrO_4$ spinel ferrite undergoes a direct optical transition. The sample's E_g value listed in Table 3, it was compared with values for various semiconductors [65–67] and spinel materials [27,68–73]. It is important to note that materials with higher E_g energy are recognized for their ability to absorb ultraviolet (UV) photons, as shown by several semiconductor examples presented in Table 3 [60,61]. Surprisingly, when viewed alongside, to other spinel ferrites and certain semiconductors, the computed E_g value for $Li_{0.5}Co_{0.5}FeCrO_4$ sample is lower [27,65–73]. However, a little E_g value enhances the absorption of visible light in photocatalytic reactions, making our specimen a promising candidate for visible light absorption [48]. Besides, the E_g value decreases from 3.41 eV for the undoped $Li_{0.5}Fe_{2.5}O_4$ sample to 1.85 eV for our material, consistent with the findings in Ref [27]. The E_g energy is influenced by serval item like grain size, structural characteristics and impurity ratio, it generally decreases with increasing grain size [74]. In the present study, the number of grain boundaries minimizes as the grain size elevates when Co^{2+} and Cr^{3+} are added into $Li_{0.5}Fe_{2.5}O_4$ ferrite. So, a decrease in grain boundaries results a reduced scattering of charge carriers at these interfaces, thereby minimizing carrier scattering impacts and lowers the E_g energy. Furthermore, larger grain sizes help suppress quantum confinement effects, contributing further to the reduction of the band gap. As a result, the E_g value of $Li_{0.5}Co_{0.5}FeCrO_4$ sample is lower compared to that of the undoped $Li_{0.5}Fe_{2.5}O_4$ ferrite [27]. It is apparent that the incorporation of Co and Cr elements in $Li_{0.5}Fe_{2.5}O_4$ clearly lowers its band gap energy, which improved its optoelectronic properties. Notably, the E_g value of our specimen surpasses the minimum energy threshold for water splitting ($E_g > 1.23$ eV). Therefore, the $Li_{0.5}Co_{0.5}FeCrO_4$ compound can also function as a photocatalytic material [74].

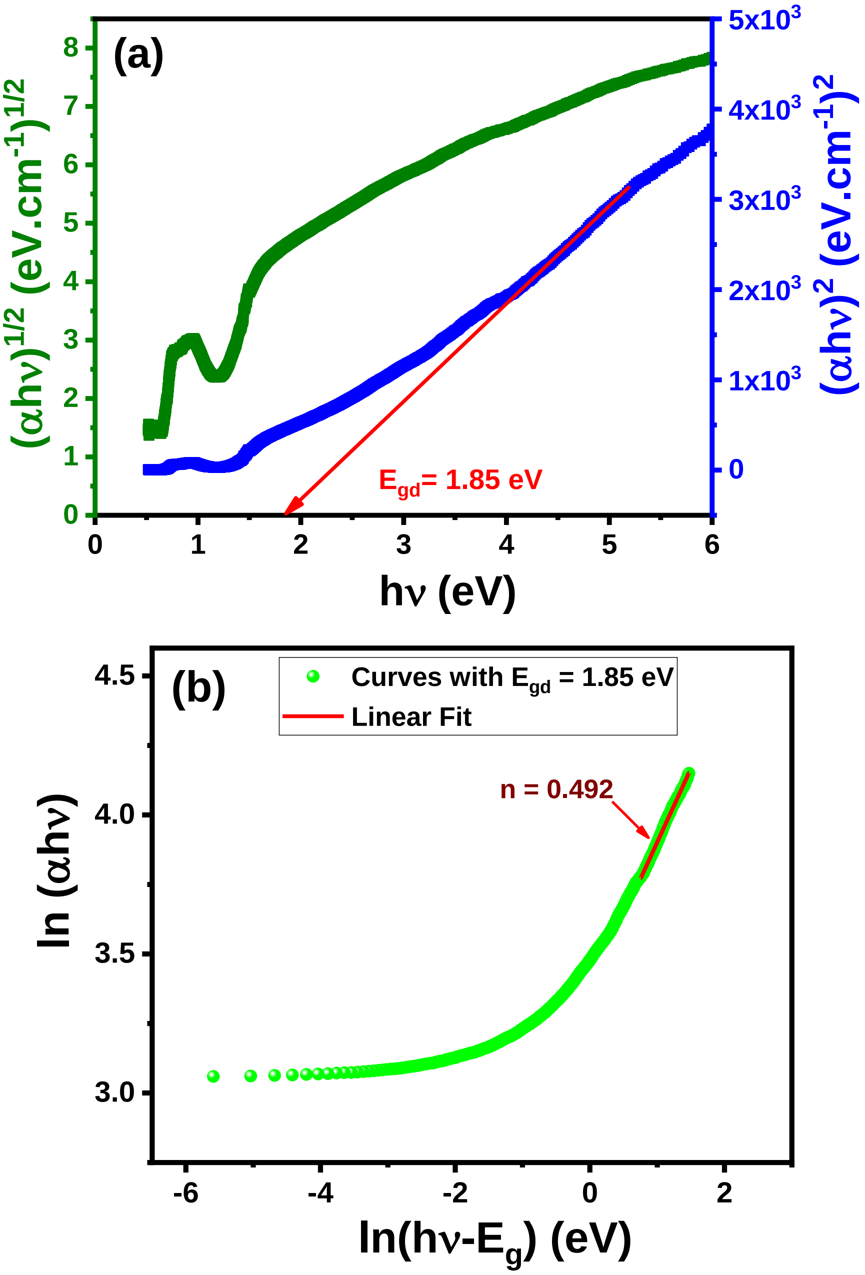

Figure 8. **(a)** Plots of $(\alpha h\upsilon)^{1/2}$ and $(\alpha h\upsilon)^2$ versus $h\upsilon$ for $Li_{0.5}Co_{0.5}FeCrO_4$. **(b)** Plot of $\ln(\alpha h\upsilon)$ versus $ln(h\upsilon-E_g)$.

Table 3. Band gap energy for $Li_{0.5}Co_{0.5}FeCrO_4$ ferrite sample compared to those reported in previous works.

Sample	Band gap energy (eV)	Reference
TiO_2	3.20	[65]
ZnO	3.37	[66]
CuO	3.85	[67]
$CoFe_2O_4$	2.60	[68]
$Cu_{0.4}Mg_{0.4}Co_{0.2}FeCrO_4$	1.88	[69]
$CoCr_2O_4$	3.07	[70]
$Li_{0.5}Fe_{2.5}O_4$	3.41	[27]
$LiNi_{0.5}Fe_2O4$	3.00	[27]
$Li_{0.2}Co_{0.3}Zn_{0.3}Fe_{2.2}O_4$	2.51	[71]
$LiMn_{0.5}Fe_2O_4$	3.51	[72]

$LiCd_{0.5}Fe_2O_4$	2.9	[73]
$Li_{0.5}Co_{0.5}FeCrO_4$	1.85	This work

3.4.3. Penetration Depth and Extinction Coefficient

The penetration depth (δ) quantifies the depth to which light can move through a specimen. By applying relation (38), (δ) can be achieved as **[75]**:

$$\delta = \frac{1}{\alpha(\lambda)} \tag{38}$$

The $\delta(\lambda)$ data for the $Li_{0.5}Co_{0.5}FeCrO_4$ specimen reveals discrete zones with changes associated with the absorption coefficient, as illustrated in Fig. 9a. In area I, the material fully blocks UV-Vis radiation, suggesting its potential as an ultraviolet filter [76]. As the spectrum moves toward area II , δ values grows, which appears a sharp band at 1025 nm . For area III, δ values continue to rise gradually up to 2400 nm, with a prominent sharp band emerging around 1926 nm.

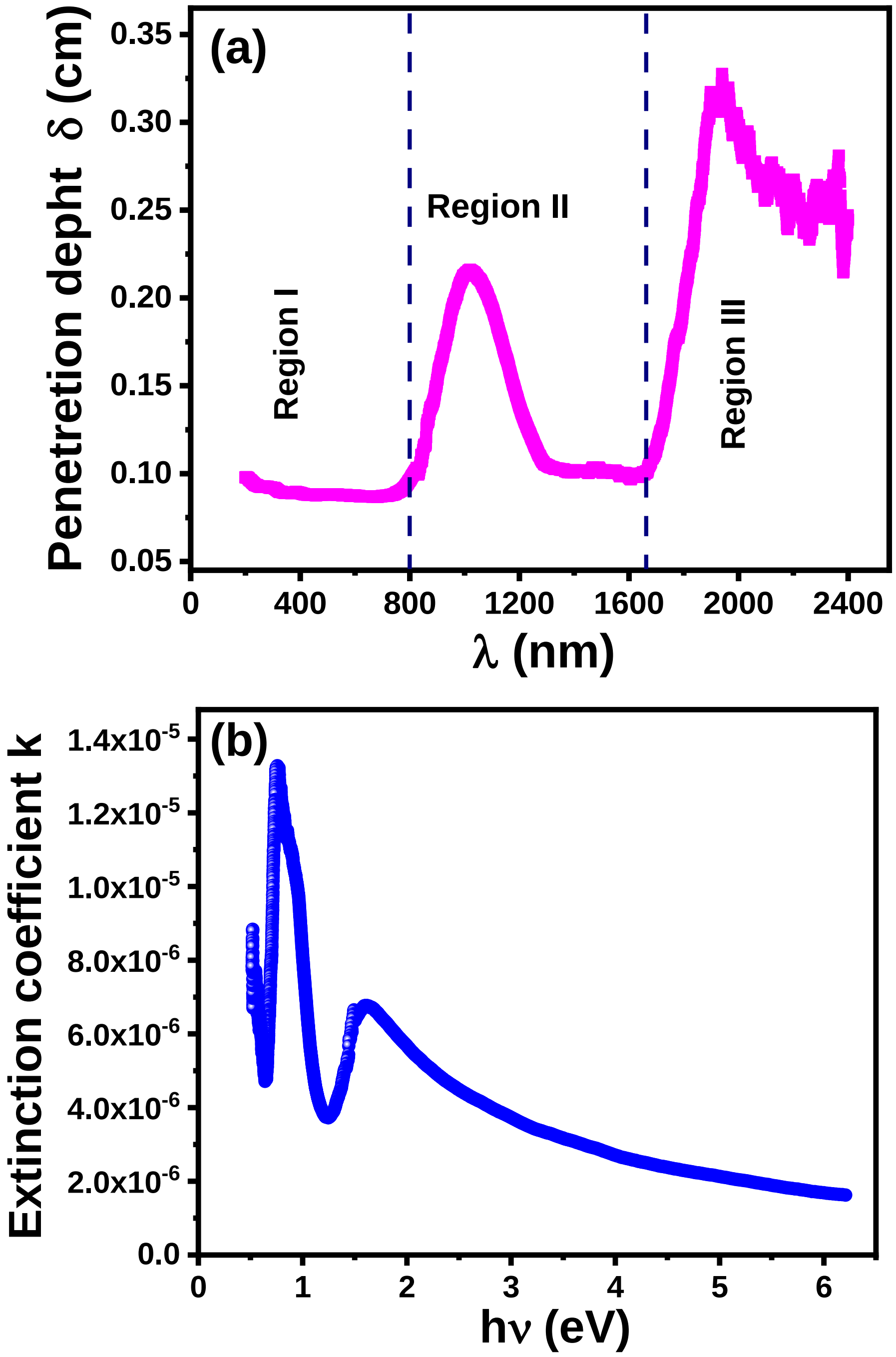

doi:10.20944/preprints202501.0641.v1

Figure 9. (a) Penetration depth (δ) vs. λ and **(b)** Extinction coefficient (k) vs. $h\nu$ for $Li_{0.5}Co_{0.5}FeCrO_4$ sample.

The extinction parameter denotes as "k" represents a material's ability to absorb and scatter light, indicating how effectively it attenuates the intensity of incident radiation. The (k) parameter is find by taking formula (39) **[77]**:

$$k = \frac{\alpha\lambda}{4\pi} \tag{39}$$

By linked to Fig. 9b, the "k" values for our compound drop as the energy ($h\nu$) grows. This decline points to reduce light absorption and scattering near the material's surface, which could be attributed to surface effects or specific electronic transitions at lower energy levels suggests diminished light absorption and scattering near the material's surface. Comparable behavior, where k values decrease with rising photon energy, has been observed in other materials [48, 78], showing that the $Li_{0.5}Co_{0.5}FeCrO_4$ ferrite allows incident light to pass through with minimal attenuation. The alterations in k values are within an interval 10^{-5} to 10^{-6}, revealing that there is little scattering and absorption loss. This feature shows the high transparency of our sample. Fundamentally, these results are consistent with previous studies by Mott and Davis [79], further validating our work.

3.4.4. Urbach Energy

The level of disorder and defects in a compound may be defined[48,78 through optical spectroscopy and the Urbach energy (E_u) data [80]. It gives insights into the band gap's confined states and the expansion of electronic transitions. Further, a little E_u value signifies a more ordered material with fewer defects, while a superior E_u value indicates more density of defects and a greater disorder. Via the photon energy ($h\nu$), the (E_u) value may be computed as follows [81]:

$$\alpha = \alpha_0 \exp\left(\frac{h\nu}{E_u}\right) \tag{40}$$

Here, α denotes the absorption coefficient, and α_0 stands for a constant. As such, it is possible to use Eq (41) to compute the E_u value.

$$ln\alpha = ln\alpha_0 + \frac{h\nu}{E_u} \tag{41}$$

So far, when examining experimental (E_u) data, formula (36) is frequently utilized. In Fig 10a, the calculated E_u value of 0.416 eV for our compound (see Table 4) was derived from the [ln(α) vs. ($h\nu$)] change. Fig 10a clearly shows a low E_u energy, which can be linked to the greater grain size present in our specimen. The decline in E_u energy, linked to the larger grain size, outlines a diminution in structural disorder and defects within the specimen. [82]. An increase in grain size, the specimen's crystalline structure is made continuous and coherent, also, minimized structural deficiencies like grain boundaries and defects. As a result, the reduced appearance of defects and enhanced structural integrity can be detected by the relatively small E_u value. The steepness parameter's value $S(T)$ and the Urbach energy (E_u) are connected by a mathematical equation as follows [83]:

$$E_u = \frac{k_B T}{S(T)} \tag{42}$$

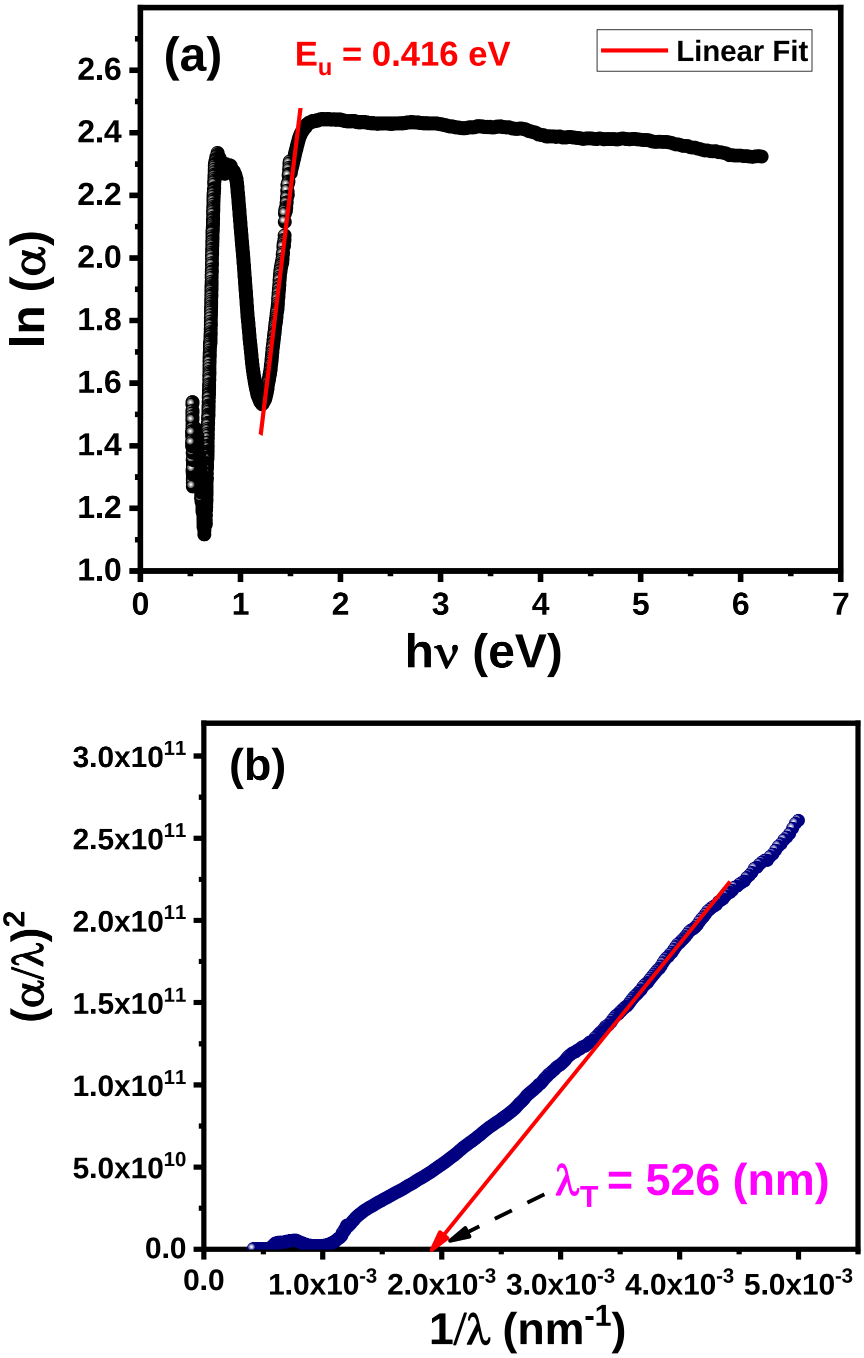

Figure 10. (a) Plot of ln(α) vs. $h\nu$ for $Li_{0.5}Co_{0.5}FeCrO_4$. **(b)** The curve of $(\alpha/\lambda)^2$ vs. $1/\lambda$.

Here, k_B stands for the Boltzmann constant, and T =300 K. In accordance with ref [63], the expanded of the absorption edge brought on by interactions between electrons and phonons or excitons and phonons is explained by the steepness parameter $S(T)$. Also, it examines how quickly the absorption coefficient varies close to the band edge in relation to photon energy. A higher $S(T)$ value reflects a sharper absorption edge and a wider energy range which the absorption coefficient varies quite significantly. Table 4 shows that the obtained S value for our specimen is 0.062, indicating significant broadening of the absorption edge. Using Eq. (43), the electron-phonon interaction energy ($E_{e\text{-}ph}$) can be determined from the S coefficient, as [63].

$$E_{e-ph} = \frac{2}{3S} \tag{43}$$

The $E_{e\text{-}ph}$ parameter signifies the energy linked to electron-phonon interactions within the material. Thus, it is vital for evaluating the compounds electronic and thermal characteristics.

Notably, a greater tendency for energy dissipation through lattice vibrations is linked by a bigger $E_{e\text{-}ph}$ value, which also signals a stronger electron-phonon interaction. In this research, the acquired $E_{e\text{-}ph}$ value for $Li_{0.5}Co_{0.5}FeCrO_4$ was computed to be 10.75 eV (see Table 4). Additionally, in optoelectronic devices, the maximum wavelength of incident radiation, stands for λ_T, also referred to as the threshold wavelength. This parameter is essential for evaluating a specimen's suitability for such applications. The λ_T value denotes the lowest wavelength of light necessary to activate more optoelectronic processes, including absorption or emission, within the sample. We estimated the λ_T value using this relation [84]:

$$\left(\frac{\alpha}{\lambda}\right)^2 = C\left(\frac{1}{\lambda}\right) - \left(\frac{1}{\lambda_T}\right) \tag{44}$$

In this context, α stands for the absorption coefficient, λ represents the wavelength of incident radiation, and C denotes a constant. So, when relying to the fitting curve, the λ_T value is assumed to be 526 nm for our specimen given in Table 4 and in the Fig 10 b.

Table 4. The values of optical parameters for $Li_{0.5}Co_{0.5}FeCrO_4$ ferrite sample.

Sample	**$Li_{0.5}Co_{0.5}FeCrO_4$**
E_g (eV)	1.85
E_u (eV)	0.416
S	0.062
$E_{e\text{-}ph}$ (eV)	10.75
λ_T (nm)	526
n_0	1.319
n_1	0.687
n_2	0.679
E_0 (eV)	1.682
E_d (eV)	0.690
ε_{op}	1.41
$n_0^{'}$	1.187
λ_0 (nm)	571
S_0 (10^{-6} m^{-2})	0.643
$n_0^{''}$	1.10
$\chi^{(1)}$ (SI)	0.032
$\chi^{(3)}$ (10^{-14} m^2/V^2)	2.689
n_2 (10^{-13} m^2/V)	8.541
R_l	0.080
R_p (Å)	0.734
α_m (Å^3)	27.13
R_m (Cm^3/mol)	18.75

3.4.5. Refractive Index

For ferrites materiels the refractive index (n) is a key optical parameter in spectral dispersion devices, describing how light travels through a sample. Relation (45) outlines how n can be computed [85]:

$$n(\lambda) = \frac{1+R}{1-R} - \sqrt{\frac{4R}{(1-R)^2} - (k(\lambda))^2} \tag{45}$$

The $n(\lambda)$ change for the $Li_{0.5}Co_{0.5}FeCrO_4$ compound is appears in Fig. 11a. The excellent quality and compactness of our sample are indicated by the presence of significant absorption bands in the UV-VIS-NIR portions [78]. The Cauchy law provided by equation (46) is applied to model the change of $n(\lambda)$ measurement.

$$n = n_0 + \frac{n_1}{\lambda^2} + \frac{n_2}{\lambda^4} \tag{46}$$

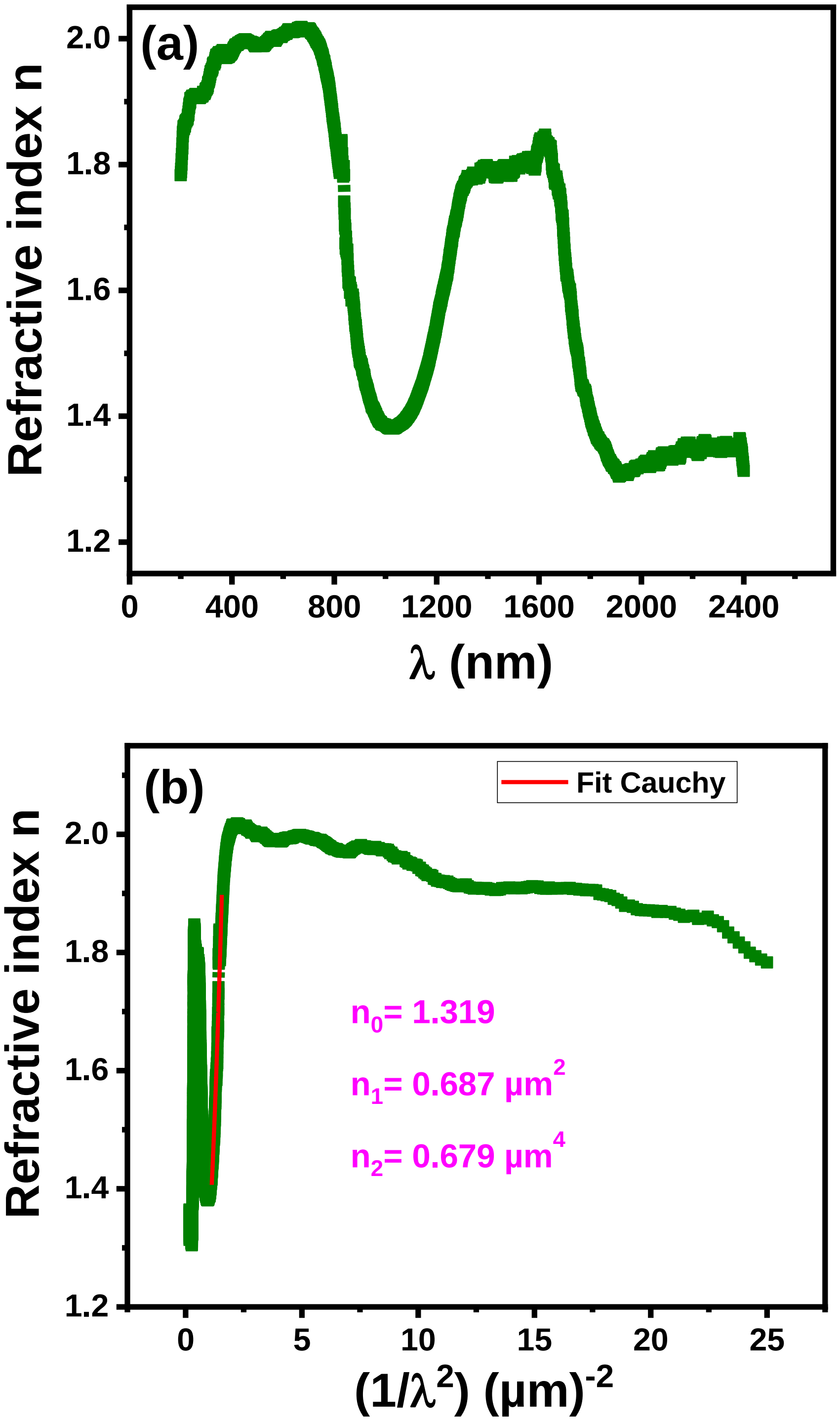

Figure 11. (a) Refractive index n versus λ for $Li_{0.5}Co_{0.5}FeCrO_4$ spinel ferrite. **(b)** The fit of $n(\lambda)$ curve using Cauchy relation.

In the preceding equation, n_0, n_1 and n_2 denotes the Cauchy parameters. Fig. 11 b shows the refractive index (n) plotted against $(\frac{1}{\lambda^2})$, as described by Eq. (46). The estimated Cauchy parameters for our sample are listed in Table 4, offering a mathematical model of the refractive index's wavelength dependence. Being aware these factors is crucial to knowing light propagation and spectrum dispersion within the samples.

The single oscillator (E_0) and dispersion (E_d) energies that characterize the intensities of interband optical transitions may be determined via the Wemple-Didomenico formula (Eq. 47) [86]. The parameters above, including the refractive index (n), the single oscillator energy (E_0), the dispersion energy (E_d), and the photon energy ($h\upsilon$), were related using this formula:

$$n^2 - 1 = \frac{E_0 E_d}{E_0^2 - (h\upsilon)^2} \tag{47}$$

The values of E_0 and E_d were obtained from the $\left[\left(\frac{1}{n^2-1}\right) \text{ vs.} (h\upsilon)^2\right]$ change, as displayed in Fig. 12a and Table 4. By integrating Eq. (48) with the computed E_0 and E_d values, we can obtain the static refractive index (n'_0) and the zero-frequency dielectric constant (ε_{op}):

$$\varepsilon_{op} = n'^2_0 = 1 + \frac{E_d}{E_0} \tag{48}$$

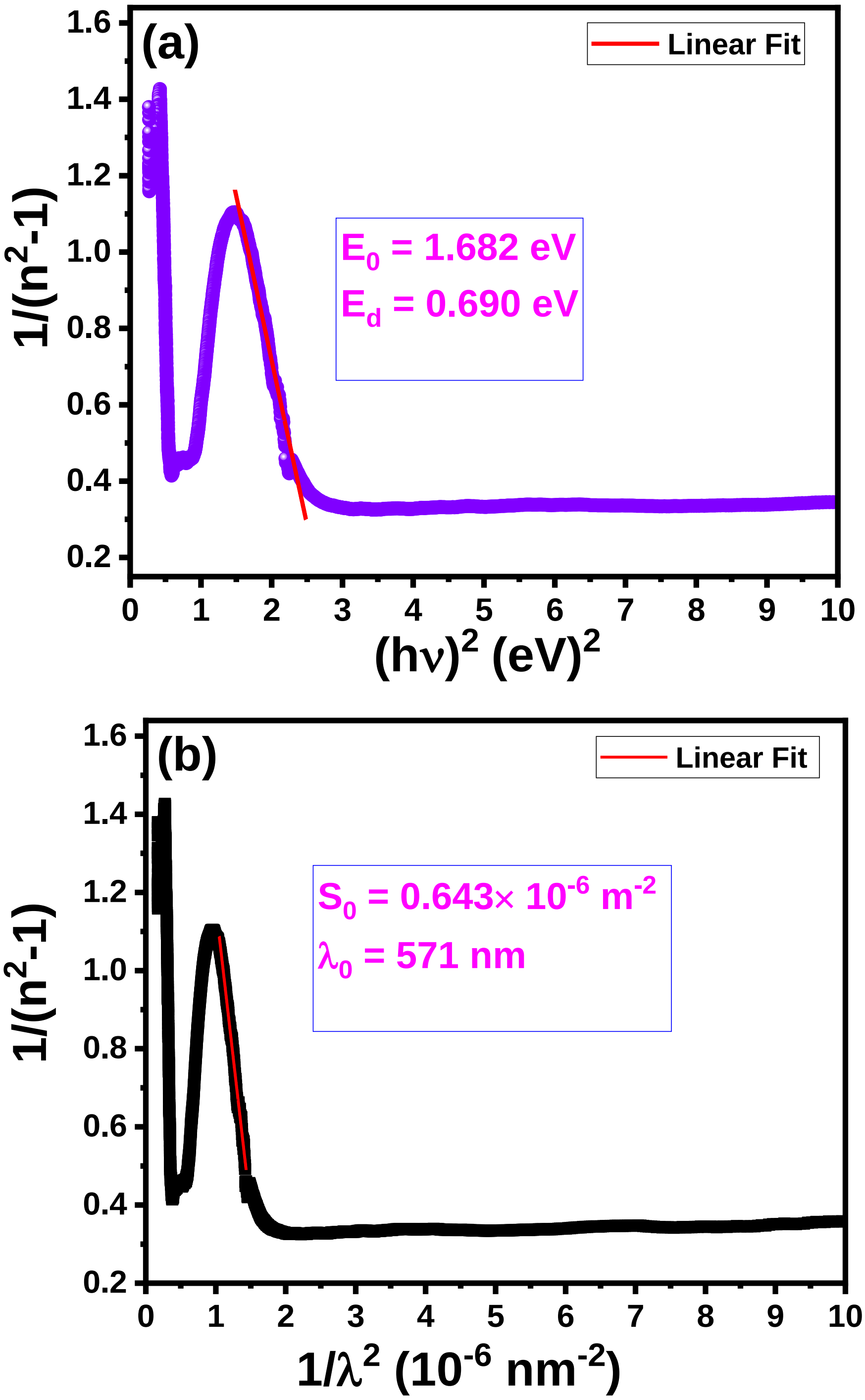

Figure 12. (a). Plot of $1/(n^2-1)$ versus $(h\nu)^2$ for $Li_{0.5}Co_{0.5}FeCrO_4$ spinel ferrite. **(b)** Plot of $1/(n^2-1)$ versus $(1/\lambda^2)$ for $Li_{0.5}Co_{0.5}FeCrO_4$ spinel ferrite.

Table 4 displays the computed values for our compound, which are $\varepsilon_{op} = 1.41$ and $n'_0 = 1.187$. Interestingly, the n_0 value derived from the Cauchy fit closely resembles the computed static refractive index (n'_0). This agreement illustrates the dependability and consistency of the outcomes obtained using various approach methods. By applying relation.(49), various parameter such as the average oscillator strength (S_0) and the oscillator wavelength (λ_0) for the $Li_{0.5}Co_{0.5}FeCrO_4$ ferrite were found as follows **[87]**.

$$\frac{1}{n^2-1} = \frac{1}{S_0\lambda_0^2} - \frac{1}{S_0\lambda^2} \tag{49}$$

Fig. 12b depicts the change of $\left(\frac{1}{n^2-1}\right) vs \ \frac{1}{\lambda^2}$. From this data, the parameter λ_0 was found to be 571 nm, and the S_0 value was computed to be 0.643×10^{-6} m^{-2} for our specimen (see Table 4). The average oscillator strength and characteristic wavelength of optical transitions in the spinel material are revealed by these measurements, which are essential for comprehending their optical characteristics and electrical structure. The static refractive index (n''_0) can also be obtained in this way [88,89]:

$$n''^2_0 - 1 = \lambda_0^2 S_0 \tag{50}$$

In this regard, the expected value of n''_0 was found to be 1.10, this correlates well with those acquired from the Cauchy adjustment and the results derived from E_0 and E_d.

3.4.6. Optical Conductivity and Optical Dielectric Constants

In this phase, we have assessed the optical conductivity ($\sigma_{op}(\lambda)$), complex optical permittivity ($\varepsilon(\lambda)$), real and imaginary components ($\varepsilon_1(\lambda)$), ($\varepsilon_2(\lambda)$), and optical loss factor ($\tan(\delta)$) for the $Li_{0.5}Co_{0.5}FeCrO_4$ ferrite. These findings were computed using the following way [90–92].

$$\sigma_{opt} = \frac{\alpha(\lambda)n(\lambda)c}{4\pi k(\lambda)} \tag{51}$$

$$\varepsilon(\lambda) = [n(\lambda) - ik(\lambda)]^2 = \varepsilon_1(\lambda) - i\varepsilon_2(\lambda) \tag{52}$$

$$\varepsilon_1(\lambda) = n^2(\lambda) - k^2(\lambda) \tag{53}$$

$$\varepsilon_2(\lambda) = 2n(\lambda)k(\lambda) \tag{54}$$

$$\tan(\delta) = \frac{\varepsilon_2(\lambda)}{\varepsilon_1(\lambda)} \tag{55}$$

The material's capacity for carrying light or electromagnetic radiation is measured by its optical conductivity denotes as $\sigma_{op}(\lambda)$. As represents in Fig. 13a, the ($\sigma_{op}(\lambda)$) values were greater at shorter wavelengths and lower at longer wavelengths, indicating a strong photo-response of the spinel ferrite. This suggests that the material is more sensitive to light with higher energy photons, likely due to electron excitation. The real part of the permittivity $\varepsilon_1(\lambda)$, which is linked to $n(\lambda)$ and $k(\lambda)$, followed a similar trend to the refractive index, as seen in Fig. 13b. Nonetheless, an insignificant rise in the imaginary portion, $\varepsilon_2(\lambda)$, was noted as the wavelength increased, indicating slight energy dissipation or absorption as the wavelength grows (Fig. 13c). These results are consistent with similar findings in other compounds and offer valuable insights into the characteristics of spinel compounds when exposed to light [75,84]. Further, when exposed to an electric or electromagnetic field, the material's energy dissipation is measured by the optical loss factor, $\tan(\delta)$. Fig. 13d shows the change of $\tan(\delta)$ for $Li_{0.5}Co_{0.5}FeCrO_4$ ferrite, which appears to rise at longer wavelengths [93].

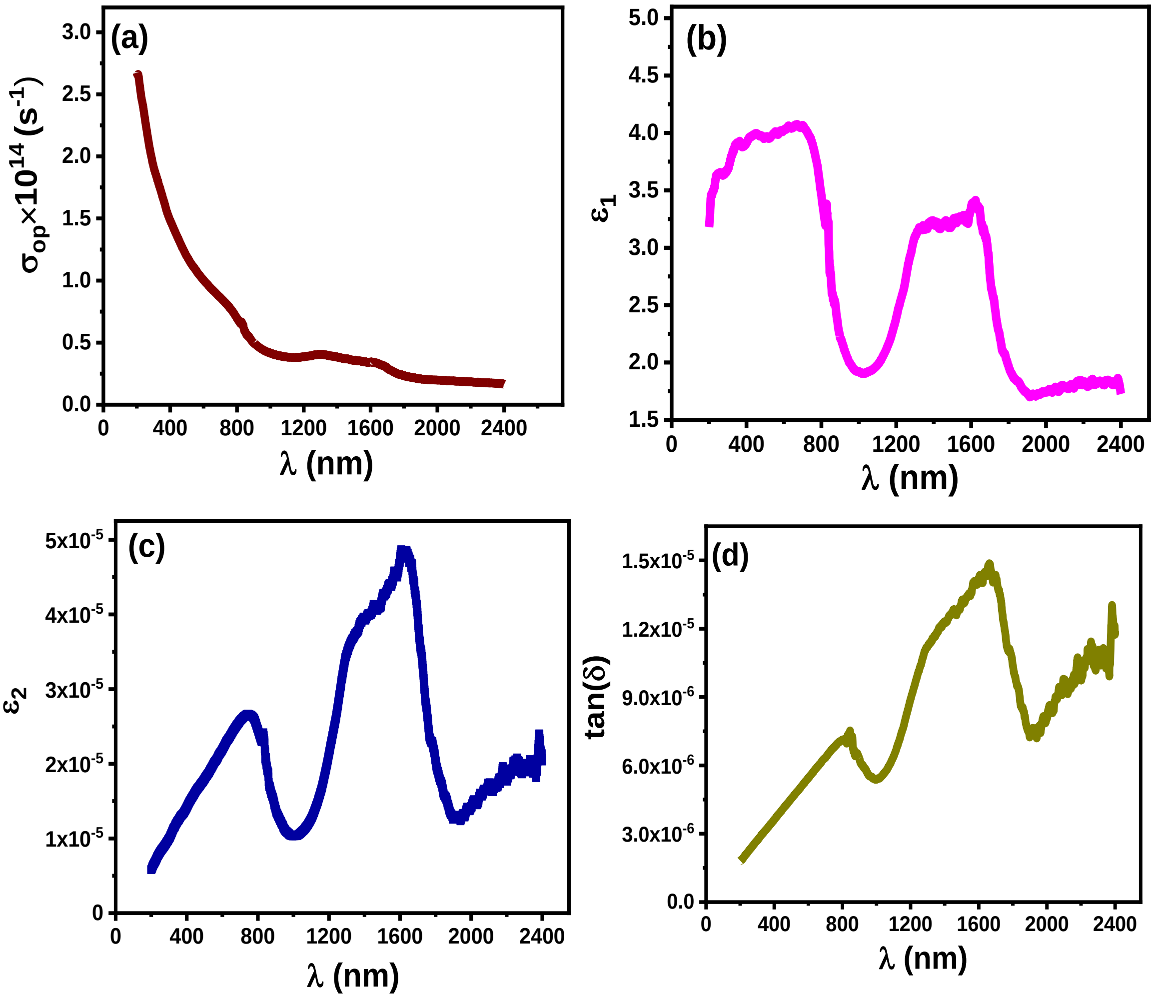

Fig. 13. **(a)** Optical conductivity (σ_{op}) versus λ for Li$_{0.5}$Co$_{0.5}$FeCrO$_4$ spinel ferrite. **(b)** Real part of dielectric permittivity $\varepsilon_1(\lambda)$. **(c)** Imaginary part of the dielectric permittivity $\varepsilon_2(\lambda)$. **(d)** Variation of the optical loss factor $\tan(\delta)$.

3.5. Theoretically Optical Parameters.

3.5.1. Reflection Loss (R_L) and Polaron Radius (R_p).

In this section , it is feasible to compute the reflection loss (R_L) through utilizing this connection [94]:

$$R_L = \left(\frac{n-1}{n+1}\right)^2 \tag{56}$$

Here, n denotes the refractive index, R_L stands for the reflection loss. As presented in Table 4, the value for R_L was estimated as $R_L = 0.080$ for Li$_{0.5}$Co$_{0.5}$FeCrO$_4$ ferrite. In our case , the reflection loss value obtained for our specimen is lower compared to the undoped Li$_{0.5}$Fe$_{2.5}$O$_4$ ferrite [95], indicating that the inclusion of Co and Cr reduces the reflection loss value . On the other hand, the polaron radius (R_p) refers to quasi-particles representing the interaction of electrons with ions in the specimen, which significantly influences its optical conductivity. It can be viewed as a self-trapped electron that moves between sites via lattice distortion. The defect levels at the nanoscale may be responsible for the polaron production in ferrite nanoparticles. Depending to their radius, polarons are categorized to be small or big in the lattice model. In ferrites materiels, lattice vibrations bring localized charge carriers closer together, leading to the formation of small polarons. The polaron radius can be determined using the appropriate calculation method as follows [96]:

$$R_p = 0.5\left(\frac{\pi}{6N}\right)^{1/3} \tag{57}$$

The number of locations per unit volume, denotes by N, in this work, the N value was obtained based to the structure of ferrites compounds, which contain 64 tetrahedral and 32 octahedral locations per unit volume, yielding, $N = 96/a^3$ N. For our specimen, the estimated polaron radius was 0.734 Å, as list in Table 4. This value is significantly smaller than all the hopping lengths between various cations in the structure (refer to Table 1). Consequently, since the polaron radius is less than the hopping lengths, it indicates the presence of small polarons in the present compound [96].

3.5.2. Molar Refractive Index (R_m) and Molar Electronic Polarizability (α_m)

The molar refractive index denotes by (R_m), the refractive index (n) and molar volume ($V_m = M_w / \rho_x$) are linked by the Lorentz–Lorenz relation in the following manner [97]:

$$R_m = \frac{n^2-1}{n^2+2} \times \frac{M_w}{\rho_x} \tag{58}$$

Here, M_w represents the molecular weight, V_m stands for molar volume and ρ_x denotes the X–ray density of our specimen.

This formula can additionally be used to find the material's molar electronic polarizability (α_m) as follows [98]:

$$\alpha_m = \frac{3R_m}{4\pi N} \tag{59}$$

From these formulae, the value of molar electronic polarizability (α_m) was determined as 27.13 Å^3, and the R_m value was found to be 18.75 (cm^3.mol^{-1}) for our specimen (see Table 4). Also, the polarizability factor reflects the compound’s ability to respond to an electromagnetic field through the displacement of its electrons. The calculated value of α_m clearly shows its direct proportionality to R_m factor. This relationship becomes important when exploring the material's non-linear optical properties, which depend on its electronic polarizability. When a light beam strikes the material, electronic polarization induces optical non-linearity. As a result, this effect is associated with various optical properties, such as the electro-optical effect, metallic ion concentration, and refractive index, which are essential for fabricating optical functional devices like memory devices, modulators, and optical sensors.

3.5.3. Non-Linear Optical Parameters

Nonlinear optics explores how light interacts with matter. Generally, a compound's optical response changes linearly with the strength of the induced electric field. However, at high power levels, the specimen's physical properties can change more rapidly, giving rise to nonlinear effects. The induced polarization for the sample is related to both linear and nonlinear susceptibilities, expressed as a series expansion of powers of the electric field intensity E, following the corresponding mathematical relation [99]:

$$P = \varepsilon_0[\chi^{(1)}E + \chi^{(2)}E^2 + \chi^{(3)}E^3 + \cdots] \tag{60}$$

In this part, $\chi^{(1)}$ denotes the linear susceptibility, while the second and third-order nonlinear susceptibilities are symbolized by $\chi^{(2)}$ and $\chi^{(3)}$.

Nevertheless, $\chi^{(2)}$ is almost insignificant in optically isotropic glasses and in crystals with a symmetry center structure, as referenced by Lines et al. [100]. Furthermore, by means of the linear refractive index, the linear optical susceptibility ($\chi^{(1)}$) may be predicted as follows:

$$\chi^{(1)} = \frac{n^2-1}{4\pi} \tag{61}$$

Yet, Miller's theory establishes a clear connection among the linear optical susceptibility $\chi^{(3)}$ and the nonlinear optical susceptibility $\chi^{(3)}$ **[101,102]:**

$$\chi^{(3)} = A[\frac{n^2-1}{4\pi}]^4 \cong A[\chi^{(1)}]^4 \tag{62}$$

In this formula, $A = 1.7\times10^{-10}$ esu represents the frequency-independent constant [102], with 1 esu is the same as 1.4×10^{-8} $m^2.V^{-2}$. In the greater wavelength level, the refractive index tends to the static refractive index (n_0'), as the value ($h\nu$) gets closer to zero, and Eq. (61), (62) take on the following form:

$$\chi^{(1)} = \frac{n_0'^2 - 1}{4\pi} \tag{63}$$

$$\chi^{(3)} \cong A[\frac{E_d}{4\pi E_0}]^4 \tag{64}$$

Through reference [101], the nonlinear refractive index n_2 may be predicted from the nonlinear susceptibility $\chi^{(3)}$.

$$n_2 = \frac{12\pi\chi^{(3)}}{n_0'} \tag{65}$$

Table 4 offers a summary of the expected values of $\chi^{(1)}$, $\chi^{(3)}$, and n_2. These characteristics' values are aligned closely with those reported for other materials regarded as promising candidates for nonlinear applications, including lasing, telecommunication, optical switching, modulators, and ultrafast optical communication [99,103].

4. Conclusions

In conclusion, the Rietveld analysis of X-ray diffraction data confirms the cubic spinel structure for the $Li_{0.5}Co_{0.5}FeCrO_4$ specimen. SEM analyses revealed that the grain size of our specimen is approximately 0.51 μm. FTIR data was employed to examine the elastic properties of the material. This analysis enabled the determination of key parameters, including elastic moduli, Pugh ratio, Debye temperature etc, which offer valuable insights into the compound's elastic behavior. Subsequently, the computed E_g value for $Li_{0.5}Co_{0.5}FeCrO_4$ sample, making our specimen a promising candidate for visible light absorption . Additionally, it is obvious that the incorporation of Co and Cr elements in $Li_{0.5}Fe_{2.5}O_4$ compound clearly lowers its band gap energy, which improved its optoelectronic properties. Our specimen shows a low E_u energy around 0.416 eV. As a result, the reduced appearance of defects and enhanced structural integrity for $Li_{0.5}Co_{0.5}FeCrO_4$ sample can be detected by the relatively smaller E_u value.

References

1. A.R. Sadrolhosseini, A.S.M. Noor, N. Faraji, A. Kharazmi, M.A. Mahdi, J. Nanomater. (2014) 8.
2. M. S¸tefanescu, T. Dippong, M. Stoia, O. S¸tefănescu, J. Therm. Anal. Calorim. 94 (2008) 389.
3. T. Dippong, E. Andrea Levei, O. Cadar, I. Grigore Deac, M. Lazar, G. Borodi, I. Petean, J. Alloy. Compd. 849 (2020) 156695.
4. T. Dippong, E.A. Levei, C.L. Lengauer, A. Daniel, D. Toloman, O. Cadar, Mater. Charact.
5. 163 (2020) 110268.
6. F. Zeb, A.R. Qureshi, K. Nadeem, M. Mumtaz, H. Krenn, J. Non Cryst. Solids 435 (2016) 69.
7. S. Pansambal, S. Ghotekar, S. Shewale, K. Deshmukh, N. Barde, P. Bardapurkar, J. Water Environ. Nanotechnol. 4 (2019) 186.
8. C.S. Pawar, M.P. Gujar, V.L. Mathe, J. Supercond. Nov. Magn. 30 (2017) 615
9. V. Dimitrov, T. Komatsu, J. Univ. Chem. Technol. Met. 45 (2010) 219.
10. M.K. Halimah, M.F. Faznny, M.N. Azlan, H.A.A. Sidek , Results Phys. 7 (2017) 589.
11. K.V. Chandekar, K.M. Kant, Phys. B Condens. Matter 545 (2018) 548.
12. T. Dippong, E.A. Levei, O. Cadar, Nanomaterials 11 (2021) 1560.
13. N.A. Tien, V.O. Mittova, B.V. Sladkopevtsev, V.Q. Mai, I.Y. Mittova, B.X. Vuong, Solid State Sciences 138 (2023) 107149.
14. M. Srivastava, S. Chaubey, A.K. Ojha, Mater. Chem. Phys. 118 (1) (2009) 174.
15. M. Mayakkannan, S. Thangarasu, V. Siva, A. Murugan, A. Shameem, S. Asath Bahadur, Materials Science and Engineering: B 306 (2024) 117448.
16. Atta Ur Rehman , Nasir Amin , Muhammad Bilal Tahir , Muhammad Ajaz un Nabi , N.A. Morley , Meshal Alzaid , Mongi Amami , Maria Akhtar , Muhammad Imran Arshad. Mater. Chem. Phys. 275 (2022) 125301
17. S.A.S. Ebrahimi, S.M. Masoudpanah, J. Magn. Magn. Mater. 357 (2014) 77.

18. N. Kouki, S. Hcini, M. Boudard, et al., RSC Adv. 9 (2019) 1990.
19. G.D. Dwivedi, K.F. Tseng, C.L. Chan, P. Shahi, J. Lourenban, B. Chatterjee, A.K. Ghosh, H.D. Yang, S. Chatterjee, Phys. Rev. B 82 (2010) 134428.
20. S.S. Ata-AlSmh, M.K. Fayek, H.A. Sayed, M. Yehia, Mater. Chem. Phys. 92 (2005) 278.
21. A.P. Surzhikov, E.N. Lysenko, E.A. Sheveleva, A.V. Malyshev, A.L. Astafyev, V.A. Vlasov, J. Electron. Mater 47 (2018) 1200.
22. Z.A. Gilani, M.S. Shifa, M.A. Khan, M.N. Anjum, M.N. Usmani, R. Ali, M.F. Warsi, Ceram. Int. 44 (2018) 1885.
23. J. Huang, H. Liu, T. Hu, Y.S. Meng, J. Luo, J. Power Sources 375 (2018) 28.
24. A. Mallick, A. Mahapatra, A. Mitra, J. Greneche, R. Ningthoujam, P. Chakrabarti, J. Appl. Phys 123 (2018) 055103.
25. H. Zeng, T. Tao, Y. Wu, W. Qi, C. Kuang, S. Zhou, Y. Chen , RSC Advances 4 (2014) 23145.
26. M. Junaid, M. A. Khan, Z. M. Hashmi, G. Nasar, N. A. Kattan and A. Laref, J. Mol. Struct., 1221 (2020) 128859.
27. N. Singh, A. Agarwal and S. Sanghi, Curr. Appl. Phys. 11 (2011) 783.
28. F. Gandomi, S.M.P. Motlagh, M. Rostami, A.S. Nasab, M.F. Ramandi, M.E. Arani, R. Ahmadian, N. Gholipour, M.R. Nasrabadi, M.R. Ganjali, J. Mater. Sci: Mater. Electron. 30 (2019) 19691.
29. J. Jing, L. Liangchao and X. Feng, J. Rare Earths, 25 (2007) 79.
30. D. Parajuli, N. Murali, V. Raghavendra, B. Suryanarayana, K.M. Batoo, K. Samatha, Appl. Phys. A 129 (2023) 502.
31. P. Sharma, P. Thakur, J.L. Mattei, P. Queffelec, A. Thakur, J. Magn. Magn. Mater. 407 (2016) 17.
32. A. Shokri, S. F. Shayesteh , K. Boustani , Ceram. Int 44 (2018) 22092.
33. S. Singhal , S. Jauhar , J. Singh, K. Chandra , S. Bansal, J. Mol. Struct 1012 (2012) 188.
34. T.R. Tatarchuk, N.D. Paliychuk, M. Bououdina, B. Al-Najar, M. Pacia, W. Macyk, A. Shyichuk, J. Alloy. Compd. 731 (2018) 1256.
35. A. Iftikhar, M.U. Islam, M.S. Awan, M. Ahmad, S. Naseem, M.A. Iqbal, J. Alloy. Compd. 601 (2014) 116.
36. Jitendra S. Kounsalye, Ashok V. Humbe, Apparao R. Chavan, K.M. Jadhav, Physica B: Condensed Matter 547 (2018) 64.
37. P.P. Hankare , R.P. Patil , U.B. Sankpal , K.M. Garadkar , R. Sasikala , A.K. Tripathi , I.S. Mulla, J. Magn. Magn. Mater. 322 (2010) 2629.
38. G. Aravind, M. Raghasudha, D. Ravinder, R.V. Kumar, J. Magn. Magn. Mater. 406 (2016) 110.
39. D.R. Manea, Swati Patil , D.D. Birajdar , A.B. Kadam, Sagar E. Shirsath, R.H. Kadam, Mater. Chem. Phys.126 (2011) 760.
40. M. Zulqarnain , S.S. Ali , M. Atif Yaqub , C.H. Wan , M.I. Khan , M. Riaz , A. Laref , M. Amami , Results Phys 61 (2024) 107732.
41. D. Gherca, A. Pui, N. Cornei, A. Cojocariu, V. Nica, O. Caltun, J. Magn. Magn. Mater. 324 (2012) 3906.
42. N. Amri, J. Massoudi, K. Nouri, M. Triki, E. Dhahri, L. Bessais, RSC Adv. 11 (2021) 13256.
43. K.A. Mohammed, A.D. Al-Rawas, A.M. Gismelseed, A. Sellai, H.M. Widatallah, A. Yousif, M.E. Elzain, M. Shongwe, Physica. B. 407 (2012) 795.
44. R.D. Shannon, Acta. Cryst. A. 32 (1976) 751.
45. V.K. Lakhani, T.K. Pathak, N.H. Vasoya, K.B. Modi, Solid State Sci. 13 (2011) 539.
46. E. Oumezzine, S. Hcini, E.K. Hlil, E. Dhahri, M. Oumezzine, J.Alloy Compd. 615 (2014) 553.
47. R.D. Waldron , Physical Review. 99 (1955) 1735.
48. S.C. Watawe, B.D. Sutar, B.D. Sarwade, B.K. Chougule, Int. J. Inorg. Mater. 3 (2001) 823.
49. F. Hcini, S. Hcini, M. M. Almoneef, M. H. Dhaou, M. S. Alshammari, A. Mallah, S. Zemni, N. Lefi and M. L. Bouazizi, J. Mol. Struct. 1243 (2021) 130769.
50. F. Hcini, S. Hcini, B. Alzahrani, S. Zemni and M.L. Bouazizi, J. Mater. Sci.: Mater. Electron. 31 (2020) 14986.
51. S. Nasrin, S.M. Khan, M.A. Matin, M.N.I. Khan, A.K.M.A. Hossain, Md.D. Rahaman, J. Mater. Sci. 30 (2019) 10722.
52. S.M. Patange, S.E. Shirsath, K.S. Lohar, S.G. Algude, S.R. Kamble, N. Kulkarni, D.R. Mane, K.M. Jadhav, J. Magn. Magn. Mater. 325 (2013) 107.
53. K.B. Modi, J. Mater. Sci. 39 (2004) 2887.
54. J. Massoudi, M. Smari, K. Nouri, E. Dhahri, K. Khirouni, S. Bertaina, L. Bessais, E.K. Hlil, RSC Adv. 10 (2020) 34556.
55. A. Gholizadeh, J. Am. Ceram. Soc. 100 (2017) 3577.
56. M.M. Wu, L. Wen, B. Y. Tang, L. M. Peng, W.J. Ding, J. Alloys. Compd. 506 (2010) 412.
57. M.A. Islam, A.K.M.A. Hossain, M.Z. Ahsan, M.A.A. Bally, M.S. Ullah, S.M. Hoque, F.A. Khan, RSC Adv. 12 (2022) 8502.

58. S.G. Algude, S.M. Patange, S.E. Shirsath, D.R. Mane, K.M. Jadhav, J. Magn. Magn. Mater. 350 (2014) 39.
59. M.B. Mohamed, A.M. Wahba, Ceram. Int. 40 (2014) 11773.
60. K.B. Modi, S.J. Shah, T.K. Pathak, N.H. Vasoya, V.K. Lakhani, A.K. Yahya, AIP Conf. Proc. 1591 (2014) 1115.
61. Y. Gao, Z. Wang, J. Pei and H. Zhang, J. Alloys Compd. 774 (2019) 1233.
62. F. Hcini, J. Khelifi, K. Khiroun, J. Inorg. Organomet. Polym 33 (2023) 3178.
63. G. Raddaoui, O. Rejaiba, M. Nasri, et al., J. Mater. Sci : Mater. Electron. 33 (2022) 21890.
64. O. Rejaiba, K. Khirouni, M.H. Dhaou, et al., Opt. Quantum Electron. 54 (2022) 315.
65. Gagandeep, K. Singh, B.S. Lark, et al., Nucl. Sci. Eng. 134 (2000) 208.
66. A. Fujishima, X. Zhang, D. A. Tryk, Surf. Sci. Rep. 63 (2008) 515.
67. J. Xie, H. Wang, M. Duan, et al., Appl. Surf. Sci. 257 (2011) 6358.
68. N.R. Dhineshbabu, V. Rajendran, N. Nithyavathy, et al., Appl. Nanosci. 6 (2016) 933.
69. D. Erdem, N.S. Bingham, F.J. Heiligtag, N. Pilet, P. Warnicke, L.J. Heyderman, M. Niederberger, Adv. Funct. Mater. 26 (2016) 1954.
70. M. L. Bouazizi , S. Hcini , K. Khirouni , M. Boudard, Optical Materials 149 (2024) 115059.
71. M.A. Kassem, A.A. El-Fadl, A.M. Nashaat, H. Nakamura, J. Alloys Compd. 790 (2019) 853.
72. F. Hcini , S. Hcini , M. Mohammed Alzahrani, M.L. Bouazizi , L. Haj Taieb, H. ben Bacha, Materials Today Communications 41 (2024) 111035.
73. I. Soudani, K. Ben Brahim, A. Oueslati, A. Aydi, K. Khirouni, A. Benali, E. Dhahri, M.A. Valente, RSC Adv. 13 (2023) 9260.
74. O. Amorri , H. Slimi , A. Oueslati , A. Aydi, K. Khirouni, Physica B 639 (2022) 414005.
75. M. L. Bouazizi, S. Hcini, K. Khirouni, F. Najar and A. H. Alshehri, J. Inorg. Organomet. Polym 33 (2023) 2127.
76. A.M. El Nahrawy, B.A. Hemdan, A.M. Mansour, A. Elzwawy, A.B. Abou Hammad, Silicon. 14 (2022) 6660.
77. A.B.J. Kharrat, K. Kahouli, S. Chaabouni, Bull. Mater. Sci. 43 (2020) 275.
78. B.A. Hemdan, A.M. El Nahrawy, A.F.M. Mansour, A.B. Abou Hammad, Environ. Sci. Pollut. Res. 26 (2019) 9508.
79. F. Hcini, S. Hcini, M.A. Wederni, B. Alzahrani, H. Al Robei, K. Khirouni, S. Zemni, M.L. Bouazizi, Physica B 624 (2022) 413439.
80. N.F. Mott, E.A. Davis, Electronic Processes in Non-crystalline Materials, Oxford university press, 2012.
81. S.A. Moyez, S. Roy, J. Nanoparticle Res. 20 (2017) 5.
82. A.M. Mansour, M. Nasr, H.A. Saleh, et al., Appl. Phys. A. 125 (2019) 625.
83. J. Dhahri, F. Hcini, S. Hcini, O. Amorri, R. Charguia, K. Khirouni, J. Sol. Gel Sci. Technol. 109 (2024) 654.
84. S. Husain, A.O.A. Keelani, W. Khan. Nano-Struct. Nano-Objects. 15 (2018) 17.
85. A. Ben Jazia Kharrat, K. Kahouli, S. Chaabouni, Bull. Mater. Sci. 43 (2020) 275.
86. A.M. Mansour, B.A. Hemdan, A.Elzwawy, A.B. Abou Hammad, A.M. El Nahrawy, Sci. Rep. 12 (2022) 9855.
87. S.H. Wemple, M. Didomenico, Phys. Rev. B. 3 (1971) 1338.
88. N. Tounsi, A. Barhoumi, F.C. Akkari, M. Kanzari, H. Guermazi, S. Guermazi, Vacuum 121 (2015) 9.
89. A.M. Ismail, M.I. Mohammed, E.G. El-Metwally, Indian J. Phys. 93 (2019) 175.
90. M.M. Abdel-Aziz, E.G. El-Metwally, M. Fadel, H.H. Labib, M.A. Afifi, Thin Solid Films 386 (2001) 99.
91. H. Yokokawa, N. Sakai, T. Kawada, M. Dokiya, Solid State Ion. 52 (1992) 43
92. R. Mguedla, A. Ben Jazia Kharrat, N. Moutia, K. Khirouni, N. Chniba-Boudjada, W. Boujelben, J. Alloys. Compd. 836 (2020) 155186.
93. Z. Raddaoui, B. Smiri, A. Maaoui, J. Dhahri, R. M’ghaieth, N. Abdelmoula, K. Khirouni, RSC Adv. 8 (2018) 27870.
94. Y. Feng, S. Lin, S. Huang, S. Shrestha, G. Conibeer, J. Appl. Phys. 117 (2015) 125701.
95. R.D. Shannon, R.X. Fischer, Phys. Rev. B Condens. Matter Mater. Phys. 73 (2006) 235111.
96. N.P. Barde , V.R. Rathod , P.S. Solanki , N.A. Shah , P.P. Bardapurkar, Appl. Surf. Sci. advences 11 (2022) 100302.
97. M.R. Eraky, S.M. Attia, Phys. B Condens. Matter. 462 (2015) 103.
98. S. Chowdhury, P. Mandal, S. Ghosh, Mater. Sci. Eng. B 240 (2019) 120.
99. W. Widanarto, M.R. Sahar, S.K. Ghoshal, R. Arifin, M.S. Rohani, K. Hamzah, M. Jandra, Mater. Chem. Phys. 138 (2013) 178.
100. A. Sharma, P. Yadav, A. Kumari, AIP Conf. Proceed. 1591 (2014) 739.
101. M.E. Lines, Phys. Rev. B 41 (1990) 3383.
102. V. Ganesh, L. Haritha, M. Anis, M. Shkir, I.S. Yahia, A. Singh, S. AlFaify, Solid State Sci. 86 (2018) 98.
103. J.J. Wayne, Phys. Rev. B 178 (1969) 1295.
104. F.Z. Rachid, L.H. Omari, H. Lassri, H. Lemziouka, S. Derkaoui, M. Haddad, T. Lamhasni, M. Sajieddine, Optical Materials 109 (2020) 110332.